Article

Immunity

Interleukin-34-dependent perivascular macrophages promote vascular function in the brain

Graphical abstract

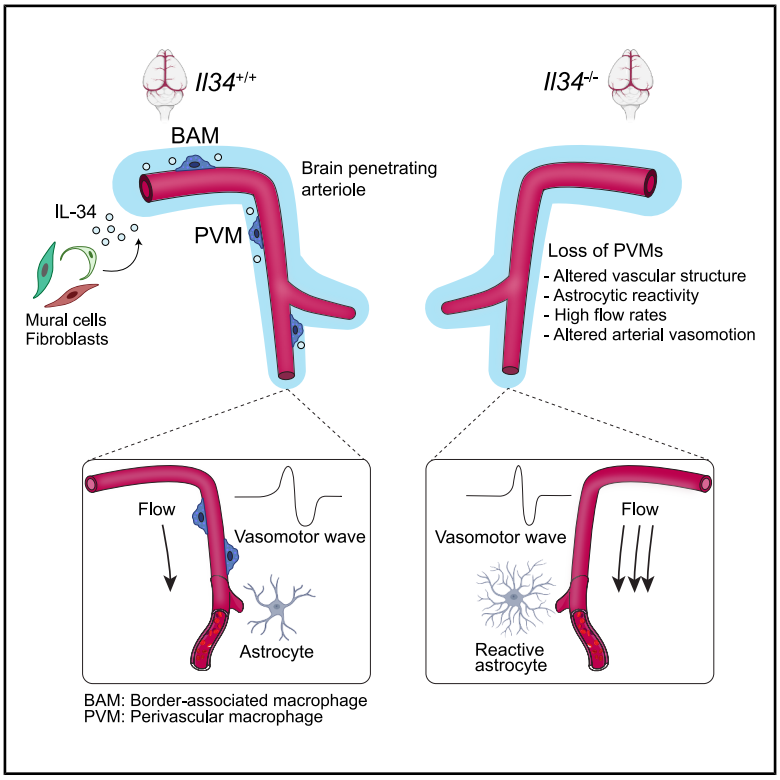

Highlights

- BAMs require CSF-1 in development, while their homeostasis in adulthood relies on IL-34
- Mural cells and fibroblasts provide the IL-34 critical for BAM maintenance
- Absence of IL-34 and/or PVMs results in altered hemodynamics in brain arterial networks

Authors

Hannah Van Hove, Chaim Glück, Wiebke Mildenberger, ..., Annika Keller, Mohamad El Amki, Melanie Greter

Correspondence

greter@immunology.uzh.ch

In brief

The niche signals critical for the homeostasis and functions of the brain border-associated macrophages (BAMs) are not well understood. Van Hove et al. demonstrate that BAMs require IL-34 derived from mural cells and perivascular fibroblasts for their maintenance in adulthood. They show that BAMs are required to promote normal vascular function in the brain.

Van Hove et al., 2025, Immunity *58*, 1–17
May 13, 2025
https://doi.org/10.1016/j.immuni.2025.04.003

CellPress

Immunity

CellPress
OPEN ACCESS

Article

Interleukin-34-dependent perivascular macrophages promote vascular function in the brain

Hannah Van Hove,[1,13] Chaim Glück,[3,13] Wiebke Mildenberger,[1,13] Ekaterina Petrova,[1,14] Upasana Maheshwari,[2,14] Philipp Häne,[1] Victor Kreiner,[1] Mitchell Bijnen,[1] Caroline Mussak,[1] Sebastian G. Utz,[1] Jeanne Droux,[3,4] Florian Ingelfinger,[1] Christian Ashworth,[1] Sebastian A. Stifter,[1] Elsa Roussel,[1] Iva Lelios,[1,5] Marijne Vermeer,[1] Sheng-Fu Huang,[2] Quanyu Zhou,[5,6] Zhenyue Chen,[5,6] Charlotte Calvet,[7] Soline Bourgeois,[7] Johanna Schaffenrath,[2,8] Daniel Razansky,[6,7] Jean X. Juang,[9] Kenichi Asano,[10] Pawel Pelczar,[11] Sarah Mundt,[1] Bruno Weber,[3] Susanne Wegener,[4] Sonia Tugues,[1] Christian Stockmann,[12] Burkhard Becher,[1] Annika Keller,[2,8,15] Mohamad El Amki,[3,4,15] and Melanie Greter[1,15,16,*]

[1]Institute of Experimental Immunology, University of Zurich, Zurich, Switzerland
[2]Department of Neurosurgery, Clinical Neuroscience Center, University Hospital Zurich, University of Zurich, Zurich, Switzerland
[3]Experimental Imaging and Neuroenergetics, Institute of Pharmacology and Toxicology, University of Zurich, Zurich, Switzerland
[4]Department of Neurology, University Hospital and University of Zurich, Zurich, Switzerland
[5]Institute for Biomedical Engineering and Institute of Pharmacology and Toxicology, Faculty of Medicine, University of Zurich, Zurich, Switzerland
[6]Institute for Biomedical Engineering, Department of Information Technology and Electrical Engineering, ETH Zurich, Zurich, Switzerland
[7]Institute of Physiology, University of Zurich, Zurich, Switzerland
[8]Neuroscience Center Zurich, University of Zurich and ETH Zurich, Zurich, Switzerland
[9]Department of Biochemistry and Structural Biology, University of Texas Science Center, San Antonio, TX 78229, USA
[10]Laboratory of Immune regulation, School of Life Science, Tokyo University of Pharmacy and Life Sciences, 1432-1 Horinouchi, Hachioji, Tokyo 192-0392, Japan
[11]Center for Transgenic Models, University of Basel, Basel, Switzerland
[12]Institute of Anatomy, University of Zurich, Zurich, Switzerland
[13]These authors contributed equally
[14]These authors contributed equally
[15]These authors contributed equally
[16]Lead contact
*Correspondence: greter@immunology.uzh.ch
https://doi.org/10.1016/j.immuni.2025.04.003

SUMMARY

The development of most macrophages depends on the colony-stimulating factor 1 (CSF-1) receptor, which has two ligands: CSF-1 and interleukin-34 (IL-34). While IL-34 is required for the homeostasis of microglia, the parenchymal macrophages in the central nervous system (CNS), it is unclear whether brain border-associated macrophages (BAMs) also depend on this cytokine. Here, we demonstrated that the embryonic development of murine BAMs in the choroid plexus, leptomeninges, and perivascular spaces required CSF-1, while IL-34 was critical for their maintenance in adulthood. In the brain, *Il34* was expressed by mural cells and perivascular fibroblasts, and its transgenic deletion in these cells interrupted BAM maintenance. *Il34* deficiency coincided with transcriptional changes in vascular cells, leading to increased flow velocity and vasomotion in pial and penetrating arterioles. Similarly, *Mrc1*^{Cre}*Csf1r*$^{fl/fl}$ mice lacking CD206^{+} perivascular BAMs exhibited increased hemodynamics in arterial networks. These findings reveal a crosstalk between vascular cells and CNS macrophages regulating cerebrovascular function.

INTRODUCTION

The central nervous system (CNS) contains several macrophage populations, including parenchymal microglia and border-associated macrophages (BAMs). The latter is associated with the borders of the CNS, which comprise perivascular spaces, the meninges (dura mater and leptomeninges), and the choroid plexus.[1,2] Both microglia and BAMs originate from early erythro-myeloid progenitors (EMPs) in the extra-embryonic yolk sac; these EMPs differentiate into premature macrophages that colonize the developing brain at embryonic day (E)9, giving rise to microglia and BAMs.[3–6] In adulthood, macrophages in the dura mater and subsets in the choroid plexus are gradually replaced by bone marrow-derived monocytes, while perivascular, leptomeningeal, and epiplexus macrophages in the choroid plexus largely self-maintain locally.[5,7]

BAMs can generally be identified by their expression of CD206 (*Mrc1*), CD38, and high levels of F4/80, but they exhibit

Please cite this article in press as: Van Hove et al., Interleukin-34-dependent perivascular macrophages promote vascular function in the brain, Immunity (2025), https://doi.org/10.1016/j.immuni.2025.04.003

transcriptional heterogeneity within and across borders.[1] The dura mater and choroid plexus, for example, house a subset of major histocompatibility complex (MHC) class II^{hi} and MHC class II^{lo} BAMs,[7,8] while the perivascular spaces of the CNS parenchyma contain perivascular macrophages (PVMs) that ubiquitously express CD163, CD206, and LYVE1.[5,9,10] Conversely, homeostatic microglia are negative for CD163, CD206, and LYVE1 but are characterized by the expression of the signature genes *P2ry12*, *Tmem119*, *Sall1*, and *Hexb*.[11]

As with many other tissue-resident macrophages, microglia are dependent on macrophage colony-stimulating factor (M-CSF or CSF-1) receptor (CSF-1R),[3,12–14] which signals through two ligands: CSF-1 and interleukin-34 (IL-34).[15,16] CSF-1 is critical for microglia development and for cerebellar microglia homeostasis in adulthood.[17] Conversely, IL-34 is dispensable for the generation of microglia but controls their maintenance in the adult brain, particularly in the forebrain.[18,19]

Microglia are recognized as crucial players in brain development and function, with diverse roles in neurogenesis, neural circuit formation, brain homeostasis, and regulation of synaptic plasticity.[20] The functions of BAMs at the various borders of the healthy or diseased brain are, however, less well understood. Recent studies demonstrated a neuroprotective role of BAMs in infection,[21,22] and a beneficial role for PVMs was also found in eliminating amyloid-β in cerebral amyloid angiopathy.[23] In other murine cerebrovascular disease models, PVMs contributed to the pathogenesis,[24] for example, by promoting neurovascular and cognitive dysfunction in hypertension,[25–27] cerebrovascular dysfunction induced by amyloid-β and ApoeE4,[28,29] and by mediating vascular permeability and the recruitment of granulocytes in ischemic stroke.[30] A recent study identified a role for BAMs in regulating cerebrospinal flow (CSF).[31]

The neurovascular unit (NVU) is a concept that interconnects neurons, glia, and the vasculature into a functional and structural unit.[32,33] It comprises endothelial cells (ECs) connected by closed cell-cell junctions, mural cells (MCs), including pericytes at capillaries and vascular smooth muscle cells (VSMCs) at arteries and veins, and astrocyte endfeet, the fine processes of astrocytes. In addition, perivascular spaces along penetrating arterioles and postcapillary venules contain PVMs and perivascular fibroblasts.[24] CNS ECs form the blood-brain barrier (BBB), which is regulated by neural tissue and MCs.[32,34,35] MCs regulate vasomotion, characterized by low-frequency oscillations of pial arteries and arterioles that occur independently of heart rate.[36,37] However, the role of PVMs in cerebral vascular function, including vasomotion, remains poorly defined.

Here, we analyzed the spatiotemporal cytokine dependency of BAMs using high-dimensional flow cytometry, histology, and single-cell RNA sequencing (scRNA-seq). We found that BAMs, including PVMs, depend on CSF-1 during early development and on IL-34 in adulthood. At blood vessels, IL-34 was produced by MCs and perivascular fibroblasts, promoting PVM homeostasis. Loss of *Il34* and/or PVMs led to changes in cerebral blood flow (CBF), vascular tone, and vasomotion and altered the transcriptional profile of vascular cells. Altogether, our study reveals that IL-34 and PVMs regulate vascular function in the brain.

RESULTS

BAMs require CSF-1R signaling for development and homeostasis

Microglia are dependent on CSF-1R signaling that is mediated by CSF-1 in development and IL-34 in adulthood.[3,17–19] We hypothesized that the development and maintenance of BAMs might follow a similar cytokine-dependent pattern. To analyze first whether the development of BAMs depends on CSF-1R signaling, we generated *Cx3cr1*^{CreER}*Csf1r*$^{fl/fl}$ transgenic mice, which exhibit tamoxifen-inducible deletion of *Csf1r* specifically in CX3CR1^{+} cells, including microglia and BAMs. We inactivated *Csf1r* in the CX3CR1^{+} cells of *Cx3cr1*^{CreER}*Csf1r*$^{fl/fl}$ mice during embryogenesis via tamoxifen treatment on E14.5 and E16.5. During embryogenesis and during early postnatal time points, all BAMs express CD206 as previously described,[38] while microglia were found to upregulate CD206 transiently and only early during development.[39–41] Thus, we identified BAMs as CX3CR1^{+}CD206^{+} cells and microglia as CX3CR1^{+}CD206^{-} cells (Figure S1A) at E18.5 by flow cytometry. Microglia and BAM numbers were drastically reduced in *Cx3cr1*^{CreER}*Csf1r*$^{fl/fl}$ embryos compared with control (*Csf1r*$^{fl/fl}$) embryos (Figure 1A). This demonstrated that, as with microglia,[3] the generation of BAMs during development requires CSF-1R signaling. Tamoxifen treatment of adult *Cx3cr1*^{CreER}*Csf1r*$^{fl/fl}$ mice also strongly reduced both BAMs (CD11b^{+}F4/80^{hi}) and microglia (CD11b^{hi}F4/80^{+}) (Figures 1B, S1B, and S1C). Likewise, administration of the CSF-1R inhibitor PLX5622 for 4 weeks to 2-month-old wild-type (WT) mice resulted in a sharp reduction of the numbers of microglia and BAMs (Figure S1D), as previously shown.[7,13,14] These data demonstrate that CSF-1R signaling is a prerequisite for the development and maintenance of BAMs in embryogenesis and adulthood, respectively.

Next, we investigated which CSF-1R ligand mediates the development and maintenance of BAMs. Flow cytometry analysis of *Csf1*-deficient (*Csf1*$^{-/-}$) mice revealed that microglia and BAMs were reduced in the absence of *Csf1* at E18.5 and postnatal day (P)5, but both populations mostly recovered by P23 (Figure 1C). This suggests that CSF-1 controls the development of BAMs but is not required for their maintenance during adulthood. Analysis at later time points was not possible due to severe developmental defects that render *Csf1*-deficient mice inviable.[42]

IL-34 is dispensable for early development of BAMs but is required for their maintenance in the adult brain

As shown above, the genesis of BAMs depended on CSF-1 while their maintenance postnatally was largely independent of this cytokine. We hypothesized that the other ligand for CSF-1R, IL-34, regulates BAM homeostasis in adulthood. To assess this, we analyzed *Il34*-deficient (*Il34*$^{LacZ/LacZ}$) mice by flow cytometry. Although *Il34* is already expressed during embryogenesis,[19,43] we found no difference in the number of BAMs between control (*Il34*$^{LacZ/+}$) and *Il34*-deficient (*Il34*$^{LacZ/LacZ}$) mice at embryonic and early postnatal stages, indicating that these cells developed independently of IL-34 (Figure 1D). Around P14, however, we observed a reduction of BAMs in the absence of IL-34, and this reduction became more pronounced in adult mice (Figure 1D). These data indicate that IL-34 is not critical for the

Please cite this article in press as: Van Hove et al., Interleukin-34-dependent perivascular macrophages promote vascular function in the brain, Immunity (2025), https://doi.org/10.1016/j.immuni.2025.04.003

CellPress
OPEN ACCESS

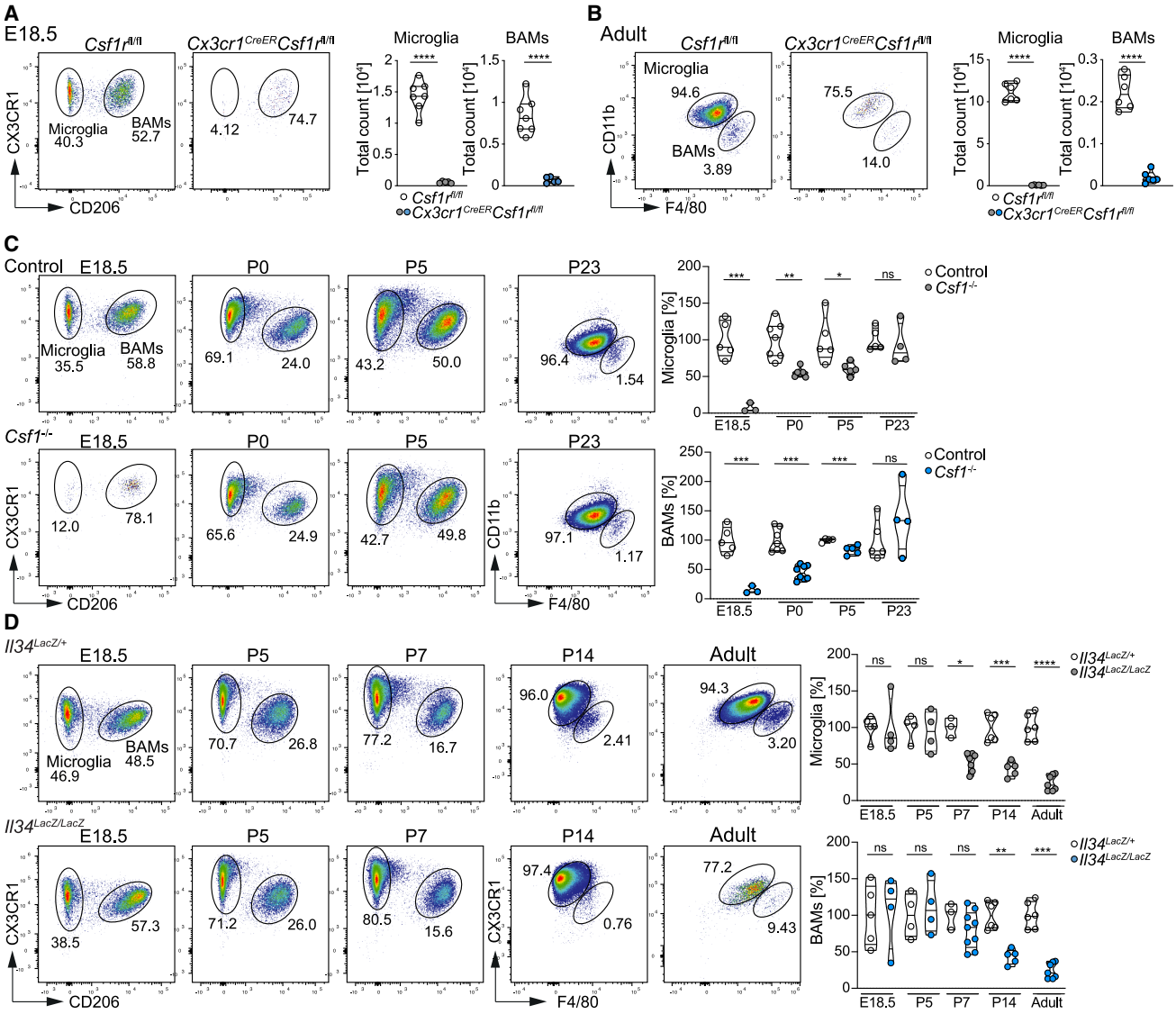

Figure 1. BAMs depend on CSF-1R signaling and require CSF-1 for their development

(A) CNS macrophages of total brain cells of tamoxifen-treated (E14.5 and E16.5) *Cx3cr1*^{CreER}*Csf1r*$^{fl/fl}$ and *Csf1r*$^{fl/fl}$ embryos were analyzed at E18.5 by flow cytometry. Shown are representative flow cytometry plots of CX3CR1^{+}CD206^{-} microglia and CX3CR1^{+}CD206^{+} BAMs and total cell numbers. Data shown were pooled from 2 independent experiments (n = 5–7).

(B) CNS macrophages (without dura mater) of adult *Cx3cr1*^{CreER}*Csf1r*$^{fl/fl}$ and *Csf1r*$^{fl/fl}$ mice were analyzed by flow cytometry 3 days after tamoxifen treatment. Shown are representative flow cytometry plots for CD11b^{hi}F4/80^{+} microglia and CD11b^{+}F4/80^{hi} BAMs and total cell numbers. Data shown were pooled from 2 independent experiments (n = 5–6).

(C) Total brain cells from control (*Csf1*$^{+/+}$ and *Csf1*$^{+/-}$) and *Csf1*$^{-/-}$ mice were analyzed by flow cytometry at E18.5, P0, P5, and P23. Representative fluorescence-activated cell sorting (FACS) plots for microglia and BAMs are shown, and cell numbers are displayed as percentages normalized to the controls. n = 3–7 from 2–3 individual experiments.

(D) Flow cytometry analysis of brain macrophages isolated from *Il34*$^{LacZ/+}$ and *Il34*$^{LacZ/LacZ}$ mice at E18.5, P5, P7, P14, and adulthood. Representative FACS plots for microglia and BAMs are shown, and cell numbers are displayed as percentages normalized to *Il34*$^{LacZ/+}$ mice. n = 4–9 from 3–4 independent experiments. In all experiments (A–D), microglia and BAMs (pregated on CD45^{+}Ly6C^{-}Ly6G^{-}CD64^{+}MerTK^{+}) were respectively gated on CX3CR1^{+}CD206^{-} and on CX3CR1^{+}CD206^{+} in mice ≤ P7 and on CD11b^{hi}F4/80^{+} and CD11b^{+}F4/80^{hi} or CX3CR1^{+}F4/80^{+} and CX3CR1^{+}F4/80^{hi} in mice > P7.

Statistical analysis was performed using Student's t tests with Welch's correction. *p < 0.05; **p < 0.01; ***p < 0.001; ****p < 0.0001; ns, not significant.

Related to Figure S1.

development of BAMs but instead controls their homeostasis in adulthood, similar to previous observations in microglia.[17–19]

To analyze which BAM subset is dependent on IL-34, we made use of high-dimensional flow cytometry followed by computational analysis. Unsupervised clustering of brain macrophages (including parenchyma, leptomeninges, and choroid plexus) derived from Il34$^{+/+}$, *Il34*$^{LacZ/+}$, and *Il34*$^{LacZ/LacZ}$ adult (6- to 8-week-old) mice revealed three main clusters of BAMs,

Please cite this article in press as: Van Hove et al., Interleukin-34-dependent perivascular macrophages promote vascular function in the brain, Immunity (2025), https://doi.org/10.1016/j.immuni.2025.04.003

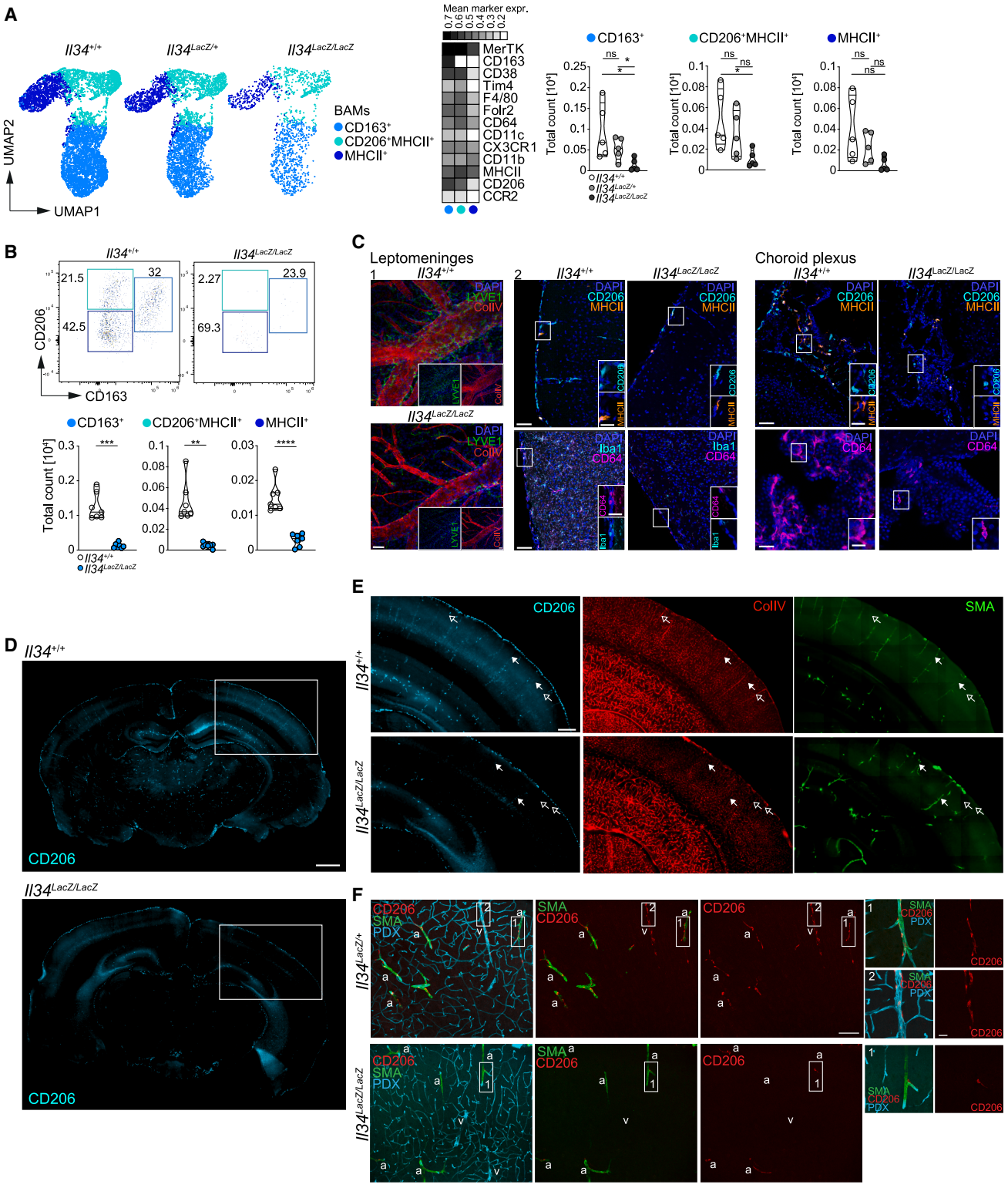

Figure 2. BAM homeostasis is dependent on IL-34

(A) Flow cytometry analysis of BAMs from total brains (without the dura mater) from adult *Il34*$^{+/+}$, *Il34*$^{LacZ/+}$, *Il34*$^{LacZ/LacZ}$ mice. (Left) High-dimensional analysis and UMAP visualization demonstrate three different BAM subsets (of Gr1^{-}Mertk^{+}CD64^{+}F4/80^{hi} cells), defined as CD163^{+}(CD206^{+}), CD206^{+}MHC class II^{+} (MHCII) and MHC class II^{+}. Data were transformed and percentile normalized. (Right) The heatmap shows the mean marker expression of markers by the respective BAM subsets. Data are normalized per column. Total counts for the different BAM subsets are derived from the UMAP. Number of cells (BAMs) per genotype used for the UMAP: *Il34*$^{+/+}$, 9,116; *Il34*$^{LacZ/+}$, 5,522; *Il34*$^{LacZ/LacZ}$, 1,529. *n* = 5 per genotype from 1 experiment.

(legend continued on next page)

Please cite this article in press as: Van Hove et al., Interleukin-34-dependent perivascular macrophages promote vascular function in the brain, Immunity (2025), https://doi.org/10.1016/j.immuni.2025.04.003

defined by differential expression of MHC class II, CD206, and CD163 (Figures 2A and S1C). $CD163^{+}CD206^{+}$ BAMs are typically classified as PVMs while $CD206^{lo/-}$ BAMs were previously described to express, for example, MHC class II and CD14 while being largely negative for CD38, CD163 (Figure S1C) and LYVE1.[7,8] The latter subset is predominantly present in the choroid plexus and the dura mater.[7,44] Each of the BAM subsets was reduced in *Il34*-deficient brains compared with $Il34^{+/+}$ or $Il34^{LacZ/+}$ brains (Figure 2A). A slight dose-dependency between $Il34^{+/+}$ and $Il34^{LacZ/+}$ mice was also observed (Figure 2A). Manual gating supported these results, showing a significant reduction in the numbers of all three BAM subsets (Figure 2B).

Next, we performed immunofluorescence with a combination of CD206, MHC class II or CD163, and/or other macrophage markers (such as Iba1, CD64, and LYVE1) to visualize BAMs residing at various border regions in WT and *Il34*-deficient brains (Figure 2C). Consistent with our unsupervised clustering analysis of flow cytometry data (Figure 2A), we found that in adult *Il34*-deficient brains total BAMs were reduced in the leptomeninges and choroid plexus (Figure 2C), as identified by Lyve1 and CD64, respectively. Equally, PVMs ($CD206^{+}$ and $CD163^{+}$ cells) in perivascular spaces along blood vessels (collagen IV $[ColIV]^{+}$) in the brain parenchyma were decreased in the absence of IL-34 (Figures 2C and S1E, respectively). Flow cytometry analysis of micro-dissected CNS border regions also demonstrated that choroid plexus and leptomeningeal macrophages were reduced in adult $Il34^{LacZ/LacZ}$ mice, whereas dural macrophages were unaffected in adult and P14 mice (Figures S1F–S1H). Overview images of CD206 immunostaining to visualize PVMs on coronal sections from adult $Il34^{+/+}$ and $Il34^{LacZ/LacZ}$ mice further indicated an overall reduction of PVMs ($CD206^{+}$) in the forebrain (Figure 2D). PVMs have been described as considerably more abundant along arterioles than venules.[41] To determine the distribution and/or reduction of PVMs along the arteriovenous axis in *Il34*-deficient mice, we used anti-ColIV (Figure 2E) and anti-podocalyxin (PDX) antibodies (Figure 2F) to stain all blood vessels and anti-alpha smooth muscle actin (SMA) for arteries, respectively (Figures 2E and 2F). In adult $Il34^{LacZ/LacZ}$ brains, PVMs were almost absent along venules and very few residual PVMs could be detected along arterioles (Figures 2E and 2F).

Microglia homeostasis in the forebrain is primarily dependent on IL-34.[17,19] To quantitatively address whether PVMs also exhibit a brain-region-specific IL-34 dependency, we separately analyzed the forebrain and the cerebellum by flow cytometry. Total BAM numbers were reduced in $Il34^{LacZ/LacZ}$ mice in both regions (Figure S1I), indicating that IL-34 dependency of BAMs is not brain-region specific. Altogether, these results demonstrate that IL-34 is necessary for the maintenance of BAMs, including PVMs, across different regions and borders of the adult brain.

MCs and perivascular fibroblasts control PVM homeostasis in the brain through IL-34

Microglia require IL-34 derived from neurons.[18,19] Here, we analyzed which cell type in the brain and/or at the NVU produces the IL-34 critical for BAM/PVM homeostasis. Published scRNA-seq data[45] show that MCs (pericytes and VSMCs) and perivascular fibroblasts express *Il34* in the adult murine brain (Figure 3A). Visualization of *Il34*-producing cells in $Il34^{LacZ/+}$ reporter mice by X-Gal staining also demonstrated vascular *Il34* expression (Figure 3B), in addition to the previously described neuronal expression.[18,19] Furthermore, anti-IL-34 antibody staining on adult brain sections derived from $Pdgfrb^{EGFP/+}$ reporter mice, in which $PDGFRB^{+}$ cells such as perivascular fibroblasts and MCs express EGFP, confirmed the presence of IL-34 at blood vessels (Figure 3C). Colocalization of IL-34 with EGFP was also detected in these reporter mice, indicating that IL-34 is produced by *Pdgfrb*-expressing cells. *Il34*-deficient $Pdgfrb^{EGFP/+}$ reporter mice served as the negative control for the IL-34 antibody for these experiments.

To assess whether vascular and vessel-associated cells in the human brain also express IL-34, we analyzed a recently published single nucleus (sn)RNA-seq dataset of the human brain vasculature.[46] Here, *IL34* was also predominantly expressed by VSMCs, pericytes, and fibroblasts (Figure 3D), resembling the murine expression pattern described above (Figure 3A). The main IL-34 receptor, CSF-1R, was specifically expressed by brain macrophages. The putative alternative IL-34 receptor, called receptor-type protein-tyrosine phosphatase zeta (PTPRZ1),[47] was largely expressed by neurons and astrocytes (Figure S2A). We also analyzed tissue derived from postmortem brain samples for the presence of IL-34 protein, using anti-GLUT1 antibody to stain the endothelium and anti-mouse immunoglobulin G1 (IgG1) as the isotype control for the IL-34 antibody. IL-34 was detected near $GLUT1^{+}$ blood vessels, indicating that also in the human brain, IL-34 is expressed at blood vessels (Figure 3E).

To assess whether IL-34 derived from these $PDGFRB^{+}$ cells (i.e., MCs and perivascular fibroblasts) is sufficient to promote PVM homeostasis, we deleted *Il34* specifically in these cells

(B) Manual gating, representative FACS plots, and quantification of total cell numbers are shown from flow cytometric analysis of the BAM subsets (pregated on $Ly6C^{-}Ly6G^{-}CD11b^{+}F4/80^{hi}$ cells) from adult $Il34^{+/+}$ and $Il34^{Lac/LacZ}$ mice. $n = 7$ from 2 independent experiments.

(C) Immunofluorescence staining of different brain compartments (leptomeninges, choroid plexus, and perivascular spaces of the cortex) from adult $Il34^{+/+}$ and $Il34^{Lac/LacZ}$ mice. Leptomeninges (1, whole mount) shows LYVE1 (green), vascular basement membrane (ColIV [red]), and DAPI (blue). (Upper row) For leptomeninges (2, coronal section) and choroid plexus, staining for CD206 (cyan), MHC class II (orange), and DAPI (blue) are shown, and (lower row) staining for Iba1 (cyan), CD64 (magenta), and DAPI (blue) are shown for the leptomeninges (2) and CD64 (magenta) and DAPI (blue) for the choroid plexus. Scale bars (leptomeninges, 2): 50 μm (25 μm in insets) and leptomeninges (1): 50 μm. Scale bars (choroid plexus): 25 μm (12.5 μm in insets). $n = 4$; images are representative of 1 out of 3 independent experiments.

(D and E) Coronal brain sections from adult $Il34^{+/+}$ and $Il34^{Lac/LacZ}$ mice. (D) shows CD206 (cyan) staining. White boxes indicate insets shown in (E). Scale bar: 1,000 μm. (E) Staining of CD206 (cyan), SMA (green) for arteries, and ColIV (red) for all blood vessels in insets from (D). Scale bar: 50 μm. Filled arrows indicate arteries and non-filled arrows indicate veins. $n = 3$; images are representative of 1 out of 4 independent experiments.

(F) Coronal sections from adult $Il34^{LacZ/+}$ and $Il34^{Lac/LacZ}$ mice. Immunofluorescence staining of CD206 (red), SMA (green) for arteries, and PDX (podocalyxin in cyan) for all blood vessels. Arteries are indicated as "a" and veins as "v." Scale bar in the main images: 100 μm and in the insets: 20 μm. $n = 4$; 4 independent experiments. Unpaired Student's t test with Welch's correction was used.

Related to Figure S1.

Please cite this article in press as: Van Hove et al., Interleukin-34-dependent perivascular macrophages promote vascular function in the brain, Immunity (2025), https://doi.org/10.1016/j.immuni.2025.04.003

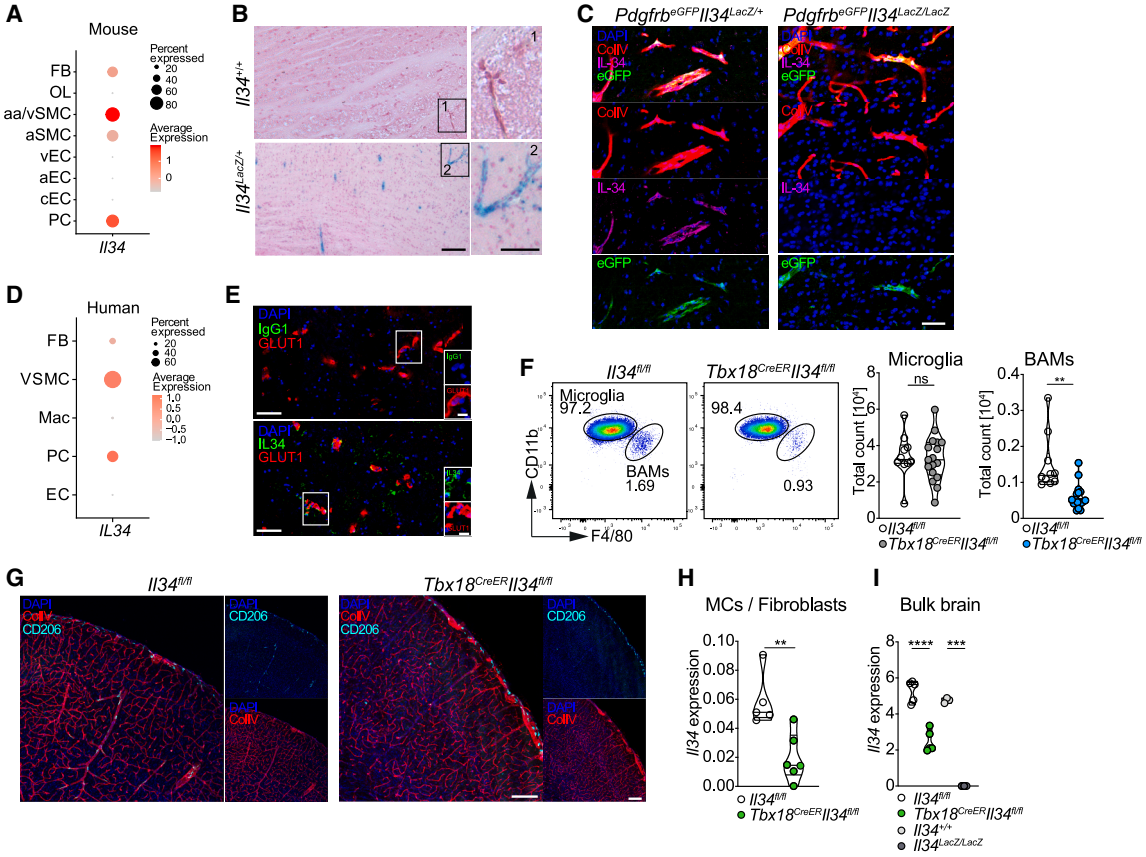

Figure 3. MCs and FB express IL-34 in the murine and human brain

(A) *Il34*-expressing cells among murine CNS vascular-associated cell types, derived from scRNA-seq data from Vanlandewijck et al.[45] The dot size represents the percentage of cells in a cluster expressing each gene; the dot color reflects the expression (as indicated in the legend). FB, fibroblasts; OL, oligodendrocytes; aa/vSMC, arteriolar/venous smooth muscle cells; aSMC, arterial smooth muscle cells; vEC, venous endothelial cells; aEC, arterial endothelial cells; cEC, capillary endothelial cells; PC, pericytes.

(B) Brain sections from adult *Il34*$^{+/+}$ and *Il34*$^{LacZ/+}$ mice stained with X-Gal. Numbered regions are enlarged areas of the main images. Scale bars: 100 μm. $n = 3$ from 2 independent experiments.

(C) Brain sections from *Pdgfrb*^{EGFP}*Il34*$^{LacZ/+}$ and *Pdgfrb*^{EGFP}*Il34*$^{LacZ/LacZ}$ mice stained with EGFP (green), CollV (red), IL-34 (magenta), and DAPI (blue). Scale bar: 50 μm. $n = 2$ from 2 independent experiments.

(D) *IL34*-expressing cells among human brain vasculature-associated cells, derived from snRNA-seq data from Yang et al.[46] FB, fibroblasts; VSMC, vascular smooth muscle cells; Mac, macrophages; PC, pericytes; EC, endothelial cells.

(E) Postmortem human brain sections were stained with anti-IL-34 (green) or IgG1 isotype control (green), anti-GLUT1 (red), and DAPI (blue). Scale bar: 50 μm, inset 25 μm. $n = 2$ from 2 independent experiments.

(F) Representative FACS plots and total cell counts of BAMs and microglia (pregated on Ly6C$^-$Ly6G$^-$CD64$^+$Mertk$^+$) in *Tbx18*^{CreER}*Il34*$^{fl/fl}$ mice and control littermates 2 weeks after tamoxifen treatment. $n = 11–17$ from 4 independent experiments.

(G) Immunofluorescent images of tamoxifen-treated *Il34*$^{fl/fl}$ and *Tbx18*^{CreER}*Il34*$^{fl/fl}$ mice stained for CD206 (cyan), CollV (red), and DAPI (blue). Scale bars, 150 μm. $n = 3$ from 2 independent experiments.

(H) *Il34* expression in FACS-sorted MCs and FBs (CD13$^+$ and/or CD140a$^+$O4$^-$ cells) derived from *Il34*$^{fl/fl}$ and *Tbx18*^{CreER}*Il34*$^{fl/fl}$ mice 2 weeks after tamoxifen treatment, assessed by RT-qPCR, normalized to *Pol2*. $n = 5–6$; data shown are pooled from 2 independent experiments.

(I) *Il34* mRNA expression in bulk brain tissue obtained from adult *Il34*$^{fl/fl}$, *Tbx18*^{CreER}*Il34*$^{fl/fl}$ (2 weeks after tamoxifen treatment), and *Il34*$^{+/+}$ and *Il34*$^{LacZ/LacZ}$ mice. $n = 3–5$ from 1 experiment.

Unpaired Student's t test with Welch's correction was performed.

Related to Figure S2.

using *Tbx18*^{CreER}*Il34*$^{fl/fl}$ mice.[48] Adult mice were treated with tamoxifen, and brains were analyzed 2 weeks later by flow cytometry. Total BAM numbers and frequency, and in particular PVMs along parenchymal vessels, were reduced in the brains of these mice (Figures 3F, 3G, and S2B), recapitulating the PVM phenotype observed in *Il34*$^{LacZ/LacZ}$ mice. Microglia were not reduced in *Tbx18*^{CreER}*Il34*$^{fl/fl}$ mice compared with control littermates, indicating that the homeostatic expression of IL-34 by neurons was not targeted (Figures 3F and S2B). These microglia also exhibited normal P2Y12 expression intensity, in contrast to *Il34*$^{LacZ/LacZ}$ mice in which P2Y12 was downregulated (Figure S2C),[17] further highlighting that microglia were not affected by *Il34* deletion in MCs and perivascular fibroblasts. Recombination of the *Il34* locus in *Tbx18*^{CreER}*Il34*$^{fl/fl}$ mice was

Please cite this article in press as: Van Hove et al., Interleukin-34-dependent perivascular macrophages promote vascular function in the brain, Immunity (2025), https://doi.org/10.1016/j.immuni.2025.04.003

CellPress
OPEN ACCESS

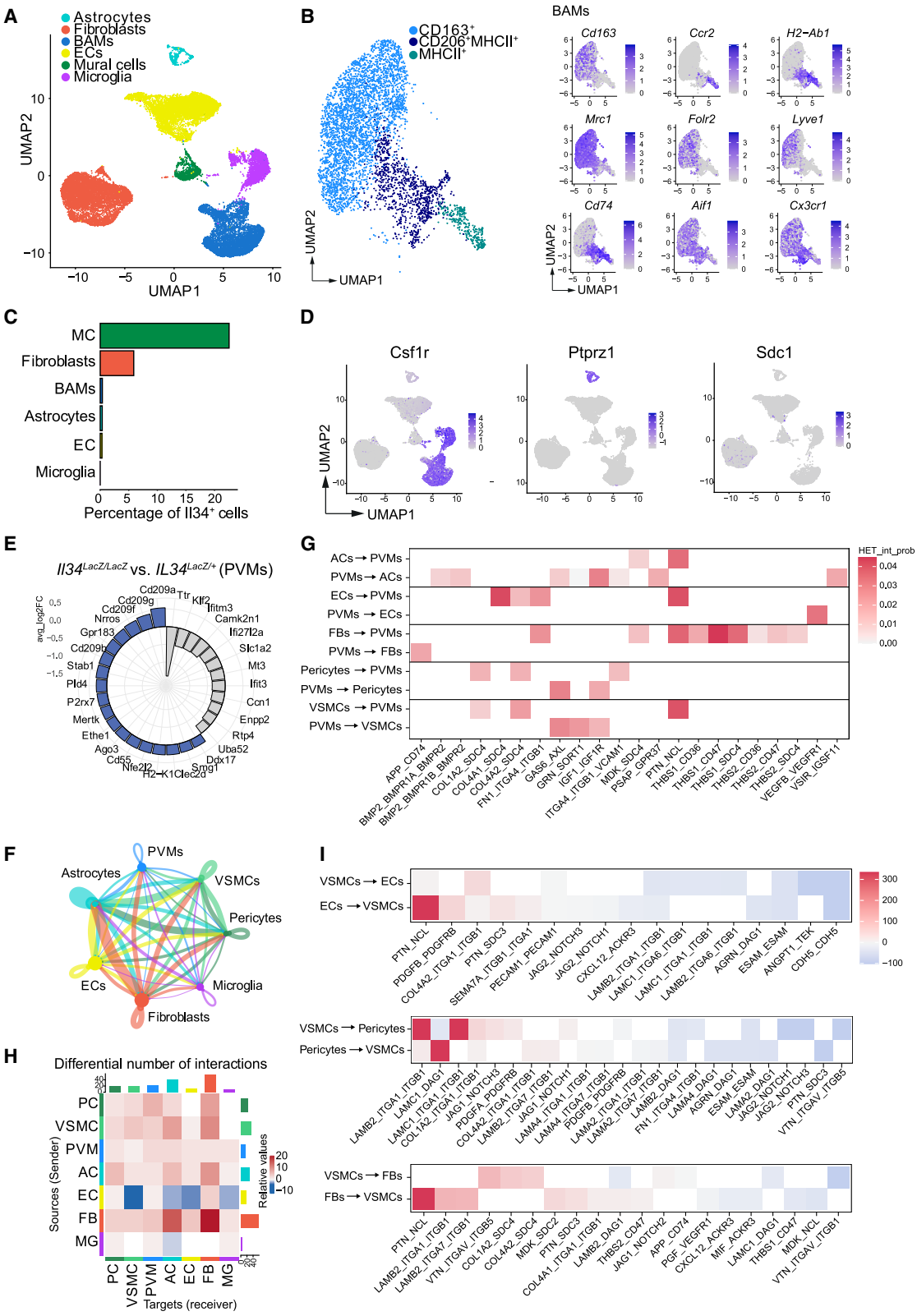

Figure 4. scRNA-seq of brain vascular-associated cells reveals changes in the absence of IL-34

(A–I) scRNA-seq of FACS-sorted mural cells (MCs) and fibroblasts (FBs) (CD13$^+$ and/or CD140a$^+$O4$^-$ cells), endothelial cells (ECs) (CD31$^+$), astrocytes (AC) (ACSA-2$^+$), BAMs (CD11b^{hi}F4/80$^+$), and microglia (CD11b$^+$F4/80^{hi}) from adult *Il34*$^{LacZ/+}$ and *Il34*$^{LacZ/LacZ}$ mice. MCs comprise both pericytes and VSMCs. ECs

(legend continued on next page)

Please cite this article in press as: Van Hove et al., Interleukin-34-dependent perivascular macrophages promote vascular function in the brain, Immunity (2025), https://doi.org/10.1016/j.immuni.2025.04.003

assessed by quantitative reverse-transcription PCR (RT-qPCR) of sorted pericytes, VSMCs, and perivascular fibroblasts ($CD13^+$ and/or $CD140a^+O4^-$), showing a deletion efficiency by approximately 70% in MCs and fibroblasts (Figure 3H). The total expression of *Il34* in the brains of these mice was significantly reduced, emphasizing the contribution of non-neuronal cells to overall *Il34* expression in the brain (Figure 3I). The number of MCs and ECs remained unaltered in $Tbx18^{CreER}Il34^{fl/fl}$ and $Il34^{LacZ/LacZ}$ mice, as quantified by flow cytometry (Figures S2D and S2E). Immunofluorescent analysis and quantification of $EGFP^+$ cells in $Pdgfrb^{EGFP}Il34^{LacZ/LacZ}$ and $PDGFRB^+$ cells in $Il34^{LacZ/LacZ}$ and control mice confirmed that *Il34*-deficiency does not result in a reduction of MCs or perivascular fibroblasts in the brain (Figures S2F and S2G). Altogether, these data indicate that, in addition to neurons, IL-34 is also produced by MCs and perivascular fibroblasts and is critical for the homeostasis of PVMs.

Loss of IL-34 alters gene expression in vascular cells

Generally, tissue-resident macrophages closely interact with stroal cells at their site of residence, which is critical for tissue homeostasis. To define a crosstalk of CNS macrophages with cerebrovascular cells and to assess the impact of *Il34*-deficiency, we performed scRNA-seq on sorted BAMs, microglia (added at a 1:10 ratio), MCs, ECs, fibroblasts, and astrocytes derived from $Il34^{LacZ/+}$ and $Il34^{LacZ/LacZ}$ whole brains (without the dura mater). Dimensionality reduction using UMAP analysis was performed on 14,000 cells per genotype, and identification of clusters was based on reported signature genes of the respective cell populations (Figures 4A and S3A).[49] MCs were separated into pericytes (*Anpep* [CD13], *Pdgfrb*, and *Cspg4*) and VSMCs (*Acta2* and *Tagln*) (Figure S3B). ECs were subclustered into arterial ECs (aECs), defined by high expression of *Bmx*, *Efnb2*, *Vegfc*, and *Sema3g*; venous ECs (vECs), by *Vwf* expression; and capillary ECs (cECs), by enriched *Tfrc* expression (Figure S3C).[45] Perivascular fibroblasts were identified by *Col1a1* expression, while astrocytes exhibited high expression of *Agt*, *Aqp4*, and *Gria2* (Figures 4A and S3A). Subclustering of BAMs revealed similar subsets we previously identified in our high-dimensional flow cytometry analysis, namely: PVMs expressing *Cd163*, MHC class II^+ BAMs expressing *H2-Ab1* and CD206 (*Mrc1*), and $MHCII^+$ BAMs expressing *H2-Ab1*, *Ccr2*, and *Cd74* (Figure 4B).

Again, *Il34* expression was restricted to MCs and perivascular fibroblasts (Figures 4C and S3D). *Csf1r* was almost exclusively expressed by the myeloid lineage, i.e., BAMs and microglia (Figure 4D).[50] The alternative IL-34 receptor *Ptprz1* was expressed by astrocytes (Figure 4D),[47] as it is largely restricted to glial cells and neuronal precursors.[51,52] Syndecan-1 (*Sdc1*), previously suggested to also bind IL-34 with low affinity,[53] was minimally expressed by fibroblasts (Figure 4D).

Differentially expressed genes (DEGs) between $Il34^{LacZ/LacZ}$ and $Il34^{LacZ/+}$ mice were found in several of these cell populations analyzed, mostly pronounced in BAMs, ECs, and fibroblasts (Figures S3E and S3F). For example, residual PVMs in $Il34^{LacZ/LacZ}$ mice showed higher expression of the C-type lectin DC-SIGN (encoded by *Cd209*), the scavenger receptor stabilin-1 (*Stab1*), and LRC33 (*Nrros*), a negative regulator of reactive oxygen species and activator of transforming growth factor β (TGF- β)[54] (Figure 4E).

Next, we employed CellChat[55] analysis to identify potential receptor-ligand interactions between PVMs and cells associated with the brain vasculature (Figures 4F and 4G). The strongest predicted interactions were observed between astrocytes and fibroblasts, VSMCs, and pericytes. PVMs were predicted to interact most strongly with VSMCs, fibroblasts, and astrocytes (Figure 4F). One of the signaling pathways between PVMs and vascular cells was the IGF1-IGF1R pathway, involving interactions between PVMs and pericytes, VSMCs and astrocytes. This pathway is known to play a role in the regulation of VSMC function and proliferation.[56,57] Additionally, the VEGFB-VEGFR1 signaling axis, which plays a role in angiogenesis and in the response to stroke,[58,59] was also predicted between ECs and PVMs (Figure 4G).

A strong reduction in the overall number of interactions between ECs and other cell types was observed in $Il34^{LacZ/LacZ}$ cells compared with $Il34^{LacZ/+}$ cells, while fibroblast interactions were increased (Figure 4H). Several pathways involved in blood vessel formation, regulation, and maintenance were altered in *Il34*-deficient mice. These included the NOTCH-signaling and PDGFRB-signaling pathways, between VSMCs and pericytes, as well as between VSMCs and ECs (Figure 4I). NOTCH3 and PDGFRB signaling are critical for the development and maintenance of MCs and play a role in regulating vascular tone and maintaining BBB integrity.[60,61] Furthermore, the loss of *Il34*

were further divided into arterial (aECs), venous (vECs), and capillary (cECs) subclusters. $n = 4$, pooled. Astrocytes (and again ECs) were sorted and sequenced in a separate experiment, followed by integration of both datasets. $n = 3$, pooled. 17,168 cells derived from $Il34^{LacZ/+}$ and 18,858 cells derived from $Il34^{LacZ/LacZ}$ mice were analyzed.

(A) UMAP representation of sequenced cell populations.

(B) Subclustering revealed 3 BAM subsets including PVMs ($CD163^+$), $MHCII^+$, and $CD206^+MHCII^+$ (left). Overlaid expression of various BAM markers to identify the different BAM subsets (right).

(C) Percentage of *Il34*-expressing cells within the respective clusters.

(D) Overlaid expression of *Csf1r*, *Ptprz1*, and *Sdc1* onto all populations (as defined in A).

(E) Differentially expressed gene (DEG) analysis of PVMs, showing the top 30 altered genes as fold change in $Il34^{LacZ/LacZ}$ mice relative to $Il34^{LacZ/+}$ mice.

(F) Circle plot illustrating the number of interactions between sorted cell populations analyzed by CellChat analysis ($Il34^{LacZ/+}$). The thickness of the colored lines correlates with the number of interactions.

(G) Heatmap of overall signaling pathways/ligand-receptors between PVMs and other populations in $Il34^{LacZ/+}$ mice, analyzed by CellChat analysis. The color code refers to the interaction probability.

(H) Heatmap shows the differential number of interactions between the cell populations of $Il34^{LacZ/LacZ}$ mice compared with $Il34^{LacZ/+}$ mice.

(I) Heatmaps of significant differential interactions between $Il34^{LacZ/+}$ and $Il34^{LacZ/LacZ}$ mice. The color code indicates the percent difference in interaction strength between $Il34^{LacZ/+}$ and $Il34^{LacZ/LacZ}$.

Related to Figure S3.

Please cite this article in press as: Van Hove et al., Interleukin-34-dependent perivascular macrophages promote vascular function in the brain, Immunity (2025), https://doi.org/10.1016/j.immuni.2025.04.003

CellPress
OPEN ACCESS

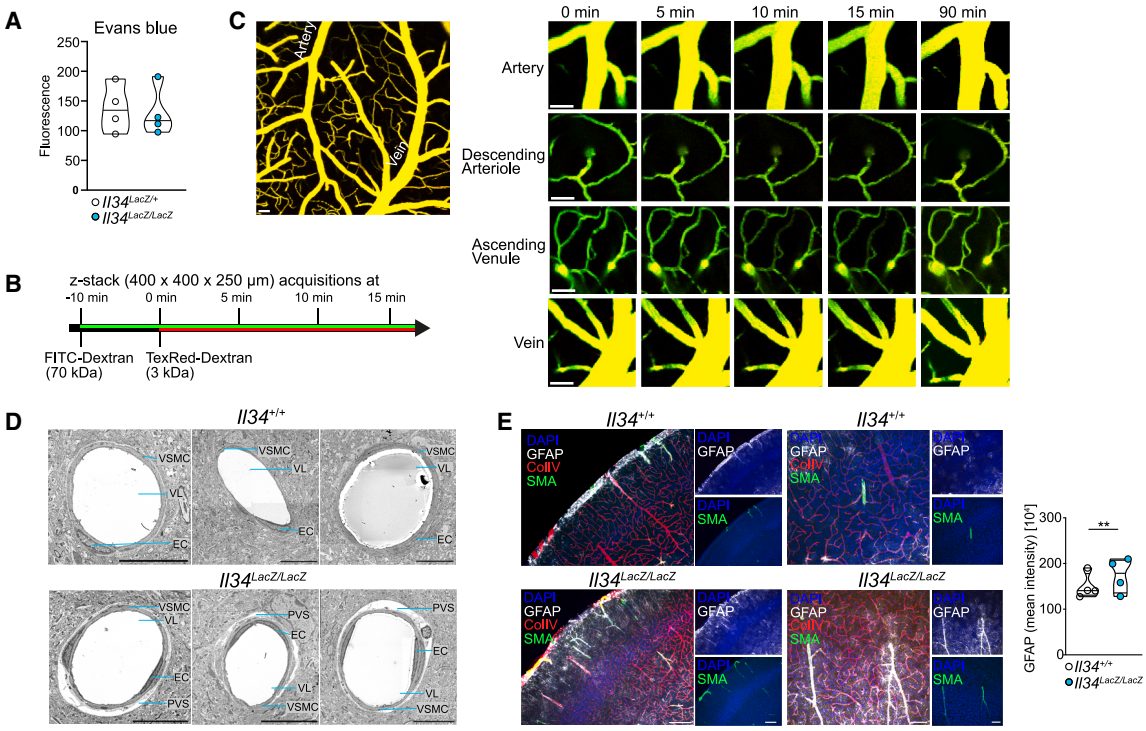

Figure 5. *Il34*-deficient mice display an altered vascular ultrastructure but do not have BBB leakage

(A) Evans blue assay of whole-brain lysates from adult *Il34*$^{LacZ/+}$ and *Il34*$^{LacZ/LacZ}$ mice 18 h post intraperitoneal (i.p.) injection. Evans blue accumulation in whole brains was measured by absorbance. $n = 4$. Unpaired Student's t test was applied.

(B and C) Assessment of vascular leakage of low molecular weight TexRed-dextran (3 kDa) in *Il34*$^{LacZ/LacZ}$ mice by two-photon imaging.

(B) Time course of z-stack acquisitions of the vasculature.

(C) On the left, a representative z-stack projection showing arterial and venous vasculature. Scale bar: 50 µm. On the right, representative vascular segments (artery, descending arteriole, ascending venule, and vein) at different time points post-injection of TexRed-dextran. Scale bar: 50 µm.

(D) TEM images from the brain (cortex) of *Il34*$^{+/+}$ and *Il34*$^{LacZ/LacZ}$ mice, showing arterioles. Scale bar: 10 µm. PVS, perivascular space; VL, vascular lumen; EC, endothelial cell; VSMC, vascular smooth muscle cell. $n = 1$.

(E) Immunofluorescence staining of *Il34*$^{+/+}$ and *Il34*$^{LacZ/LacZ}$ brain sections stained for GFAP (white), ColIV (red), SMA (green), and DAPI (blue). The mean intensity of GFAP was calculated and averaged from 3 cortical images from each brain in Fiji. Scale bar left: 150 µm (inset 75 µm), and right: 70 µm (inset 35 µm). $n = 4$, 2 experiments. Unpaired Student's t test was performed.

Related to Figure S4.

resulted in reduced *ANGPT1-TEK1* signaling between VSMCs and ECs (Figure 4I), a pathway critical for vascular maintenance and function.[62] Additionally, integrin signaling was disrupted among various vascular cell types (Figure 4I); and, angiotensin converting enzyme 2 (*Ace2*), an important regulator in blood pressure and flow,[63] was upregulated in *Il34*$^{LacZ/LacZ}$ MCs (Figures S3G and S3H). We also detected an increase of ACE2 around the bigger vessels in *Il34*-deficient mice by immunofluorescence (Figure S3I). Altogether, the changes we observed at blood vessels in the absence of *Il34* suggest dysregulation of cerebrovascular function.

Altered arteriolar ultrastructure without BBB leakage in *Il34*-deficient mice

Given that scRNA-seq data indicates altered cell-cell communication at blood vessels in the brain, we first examined whether BBB integrity might be compromised in *Il34*$^{LacZ/LacZ}$ mice. To assess this, we injected Evans blue into adult *Il34*$^{LacZ/+}$ and *Il34*$^{LacZ/LacZ}$ mice and monitored dye leakage by assessing Evans blue accumulation in whole-brain lysates. We did not detect Evans blue in the parenchyma of *Il34*-deficient mice after 18 h of circulation (Figure 5A), indicating that the BBB integrity remained largely intact in the absence of IL-34. To further confirm this *in vivo*, we used two-photon microscopy, allowing the assessment of BBB permeability across the different vascular segments, including penetrating arterioles, ascending venules, and the smallest capillaries. Fluorescently labeled dextrans of different sizes (3 and 70 kDa) were infused intravenously into *Il34*$^{LacZ/LacZ}$ mice. *In vivo* brain imaging revealed no dye leakage into the cerebral cortex; instead, the tracers remained confined within the vessel lumen (Figures 5B and 5C). In addition, *Il34*$^{LacZ/LacZ}$ mice did not display increased immune cell infiltration into the CNS parenchyma compared with controls (Figure S4A). Thus, the absence of IL-34 and/or PVMs does not alter BBB permeability.

To assess fine structural differences at the cerebrovasculature in the absence of IL-34, we performed transmission electron microscopy (TEM). We observed that the ultrastructure of ECs including endothelial cell-cell junctions appeared unaltered in the *Il34*$^{LacZ/LacZ}$ brain in comparison with the WT control

Please cite this article in press as: Van Hove et al., Interleukin-34-dependent perivascular macrophages promote vascular function in the brain, Immunity (2025), https://doi.org/10.1016/j.immuni.2025.04.003

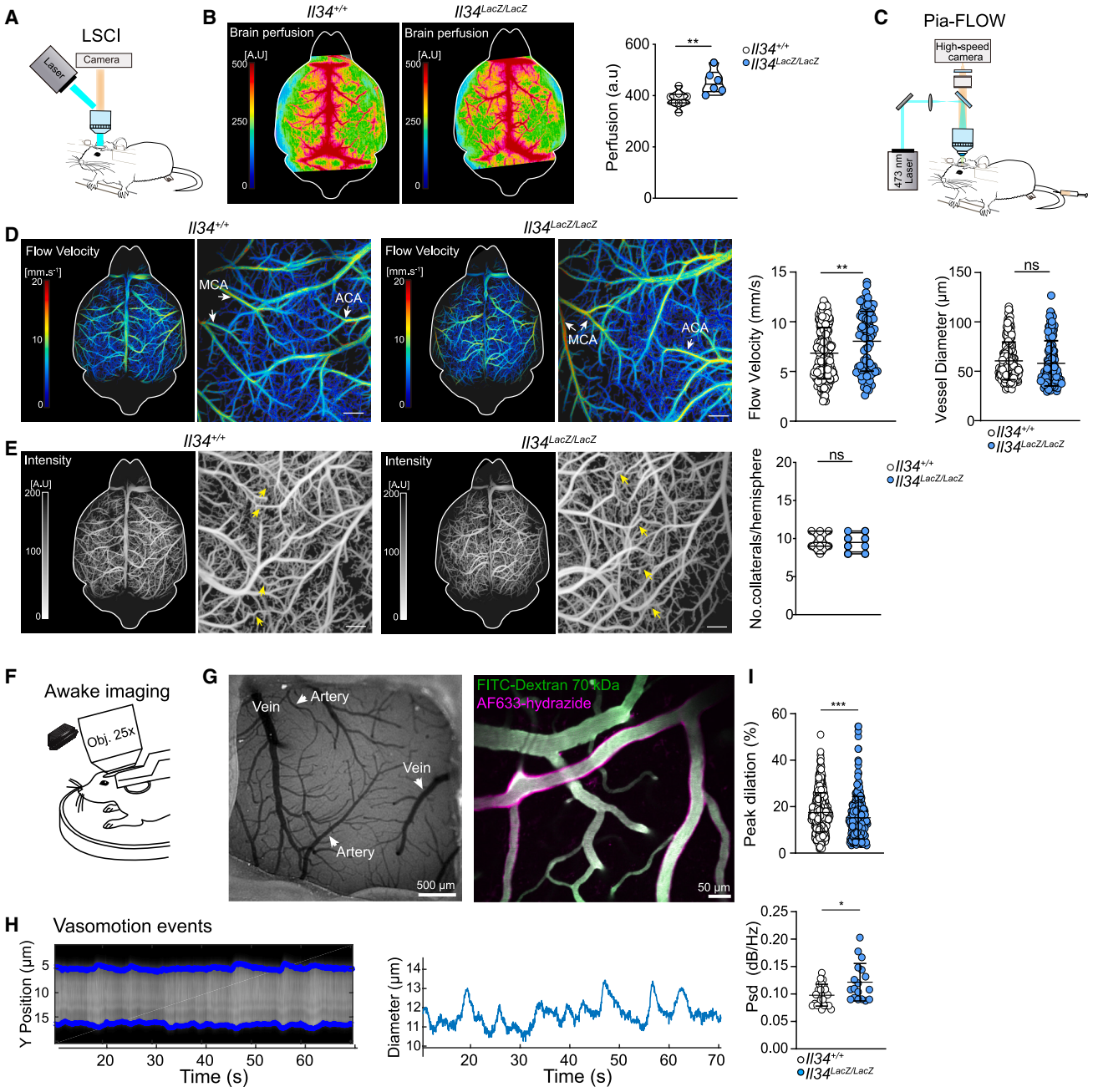

Figure 6. *Il34*-deficient mice display increased CBF and vasomotion

(A) Scheme of laser speckle contrast imaging (LSCI), related to (B).

(B) Representative LSCI showing brain perfusion in Il34$^{+/+}$ and *Il34*$^{LacZ/LacZ}$ mice (left). Quantification of brain perfusion in *Il34*$^{+/+}$ and *Il34*$^{LacZ/LacZ}$ mice (right). *n* = 6–8 from 2 independent experiments.

(C) Schematic representation of Pia-FLOW imaging, related to D.

(D) Representative Pia-FLOW images showing flow velocity in the pial vessels of *Il34*$^{+/+}$ and *Il34*$^{LacZ/LacZ}$ mice. Zoom-in images show arterial segments (middle cerebral artery [MCA] and anterior cerebral artery [ACA]) (left). Quantification of flow velocity and vessel diameters. Il34$^{+/+}$, *n* = 6 mice, 220 arterial segments; *Il34*$^{LacZ/LacZ}$, *n* = 3 mice, 83 arterial segments, related to Figure S5A.

(E) Representative Pia-FLOW intensity images showing the leptomeningeal vascular architecture of *Il34*$^{+/+}$ and *Il34*$^{LacZ/LacZ}$ mice. Leptomeningeal collaterals were identified as the tortuous anastomoses connecting the terminal distal branches between MCA and ACA and are indicated with yellow arrows (left). Quantification of leptomeningeal collaterals in *Il34*$^{+/+}$ and *Il34*$^{LacZ/LacZ}$ mice. *n* = 3–6 from 2 independent experiments (right).

(F) Schematic of awake head-fixed mouse imaging, related to (G)–(I).

(G) Representative image of a cranial window, indicating arteries and veins (left), and a two-photon image of vasculature labeled with AF633-hydrazide for arterial labeling (right).

(H) Representative image of spontaneous vasomotion events of an artery (left) with a corresponding diameter plot (right).

(legend continued on next page)

Please cite this article in press as: Van Hove et al., Interleukin-34-dependent perivascular macrophages promote vascular function in the brain, Immunity (2025), https://doi.org/10.1016/j.immuni.2025.04.003

(Figure S4B), supporting the notion of intact BBB integrity. However, notable structural alterations were detected in certain arterioles of the *Il34*$^{LacZ/LacZ}$ brain. Specifically, arteriole segments near the pial surface exhibited widened perivascular spaces and ill-defined basement membranes (Figures 5D and S4C). Additionally, VSMC were occasionally hypertrophic, and astrocyte endfeet were swollen at cortical arteriole segments (Figures S4C and S4D). These vascular abnormalities in *Il34*$^{LacZ/LacZ}$ mice were absent at the capillaries (Figure S4E).

Furthermore, increased GFAP staining on astrocytes was detected around arterioles (SMA^{+}) in the brains of *Il34*-deficient mice (Figure 5E), indicative of astrocyte reactivity generally correlating with vascular dysfunction.[64] This was further supported by the mislocalization of AQP4 in astrocyte endfeet along bigger blood vessels (Figure S4F), also commonly observed in CNS pathologies.[65] This result, along with the ultrastructural alterations in VSMCs and astrocytes, suggests that vascular function (specifically in penetrating arterioles) is altered in IL-34-deficient mice.

Il34-deficient mice display altered arterial hemodynamics and vasomotion

Next, we investigated whether the observed ultrastructural changes and the altered gene expression in the vasculature of *Il34*-deficient mice affected brain hemodynamics. We investigated first whether *Il34* deficiency impacts CBF using laser speckle contrast imaging (LSCI). This revealed that *Il34*$^{LacZ/LacZ}$ mice displayed a ~15% increase in basal cortical perfusion and CBF compared with controls (Figures 6A and 6B), indicating that a lack of IL-34 and reduction of CNS macrophages alters vascular dynamics in the brain. To specifically assess CBF changes in *Il34*-deficient mice, we used our recently established widefield fluorescence localization microscopy technique called Pia-FLOW.[66] Unlike intravital multiphoton microscopy, Pia-FLOW offers a large field of view and allows transcranial imaging of the entire vasculature, enabling horizontal visualization of pial vessels at single-vessel resolution. Consistent with the data obtained using LSCI, we observed increased flow velocity in the pial arterioles of *Il34*$^{LacZ/LacZ}$ mice compared with controls, despite no differences in vascular diameters (Figures 6C, 6D, and S5A). Overall, these data show that *Il34*-deficient mice display altered hemodynamics in the arteries, which may be partially mediated by altered PVM-VSMC interactions controlling vascular myogenic tone and resistance to flow. We also assessed whether the vascular architecture and the number of pial anastomoses in *Il34*$^{LacZ/LacZ}$ mice were altered. Although *Il34* is already expressed during embryogenesis,[43] we observed no differences in the pial vascular architecture or parenchymal vascular density (assessed by ColIV staining) in *Il34*-deficient mice (Figures 6E and S5B). These data indicate that IL-34 is not critical for the development and remodeling of the vascular architecture but regulates vascular dynamics.

Even though cerebral autoregulation maintains CBF independently of changes in blood pressure,[67] we analyzed whether the increased CBF observed in *Il34*$^{LacZ/LacZ}$ mice might result from systemic hypertension. No significant differences were found in systolic and diastolic blood pressure or blood gases between *Il34*$^{LacZ/+}$ and *Il34*$^{LacZ/LacZ}$ mice (Figures S5C and S5E). This is in agreement with a report in which PVM depletion via clodronate liposomes injected into the cerebral ventricles did not alter mean arterial pressure.[68] In line with this, we did also not detect cardiac hypertrophy as a measure for chronic hypertension in *Il34*$^{LacZ/LacZ}$, as assessed by the ratio of the heart to body weight (Figure S5D), indicating that the increased CBF observed in *Il34*$^{LacZ/LacZ}$ mice is not due to changes in the mean arterial pressure.

We next investigated whether the abnormal vascular function and perivascular spaces in *Il34*$^{LacZ/LacZ}$ mice impact arterial vasomotion. These spontaneous dilations and constrictions at low frequencies (~0.1 Hz) are known to be driven by oscillations of VSMC and occur mainly in pial arteries, arterioles, and penetrating arterioles.[36,37,69] To assess whether PVMs are implicated in spontaneous vasomotion, we investigated vasomotion in *Il34*$^{LacZ/LacZ}$ mice using *in vivo* two-photon microscopy on awake mice trained for head fixation (Figures 6F–6I). This revealed that *Il34*$^{LacZ/LacZ}$ displayed increased vasomotion in comparison with WT control mice (Figure 6I), demonstrating that PVMs support the regulation of vasomotion.

Mrc1^{Cre}*Csf1r*$^{fl/fl}$ mice display increased CBF

While *Il34*$^{LacZ/LacZ}$ mice exhibit reductions in both microglia and BAMs, we generated a mouse model (*Mrc1*^{Cre}) to specifically target CD206^{+} macrophages, including PVMs (Figure S5F). These mice were crossed with the *Csf1r*$^{fl/fl}$ strain to conditionally delete CSF-1R in CD206^{+} macrophages, leading to a significant reduction of BAMs and PVMs in the brain of adult mice (Figure 7A) but no overall changes in the numbers of other CNS-associated monocytes or neutrophils (Figure S5G). Immunofluorescent analysis of brain sections and flow cytometry analysis of the dissected borders from control and *Mrc1*^{Cre}*Csf1r*$^{fl/fl}$ mice showed specifically a reduction of parenchymal PVMs and reduced leptomeningeal macrophages (Figures 7B, S5H, and S5I), while dura mater and choroid plexus macrophages were not affected (Figures S5J–S5L).

It was previously suggested that CD206 is also transiently expressed in developing microglia at early embryonic time points.[39,41] Nevertheless, microglia numbers were not reduced in adult *Mrc1*^{Cre}*Csf1r*$^{fl/fl}$ mice (Figure 7A), demonstrating this to be a suitable and specific PVM-deficient mouse model.

In peripheral organs, the numbers of skin macrophages including dermal macrophages and Langerhans cells, and bone marrow and small intestinal macrophages were also reduced whereas macrophages in the spleen, kidney, liver, and lung were unaltered in adult *Mrc1*^{Cre}*Csf1r*$^{fl/fl}$ mice (Figure S6).

(I) Quantification of maximal dilation of spontaneous vasomotion events (top) and power spectral density (psd) of vasomotion events (bottom) in *Il34*$^{+/+}$ and *Il34*$^{LacZ/LacZ}$ mice. n = 2–4 mice.

Data are shown as mean with SD. Data normality was assessed using the D'Agostino & Pearson test. For normally distributed data, an unpaired Student's t test with Welch's correction was performed, otherwise a Mann-Whitney test was performed.

(A) and (C) are adapted from Glück et al.[66]

Please cite this article in press as: Van Hove et al., Interleukin-34-dependent perivascular macrophages promote vascular function in the brain, Immunity (2025), https://doi.org/10.1016/j.immuni.2025.04.003

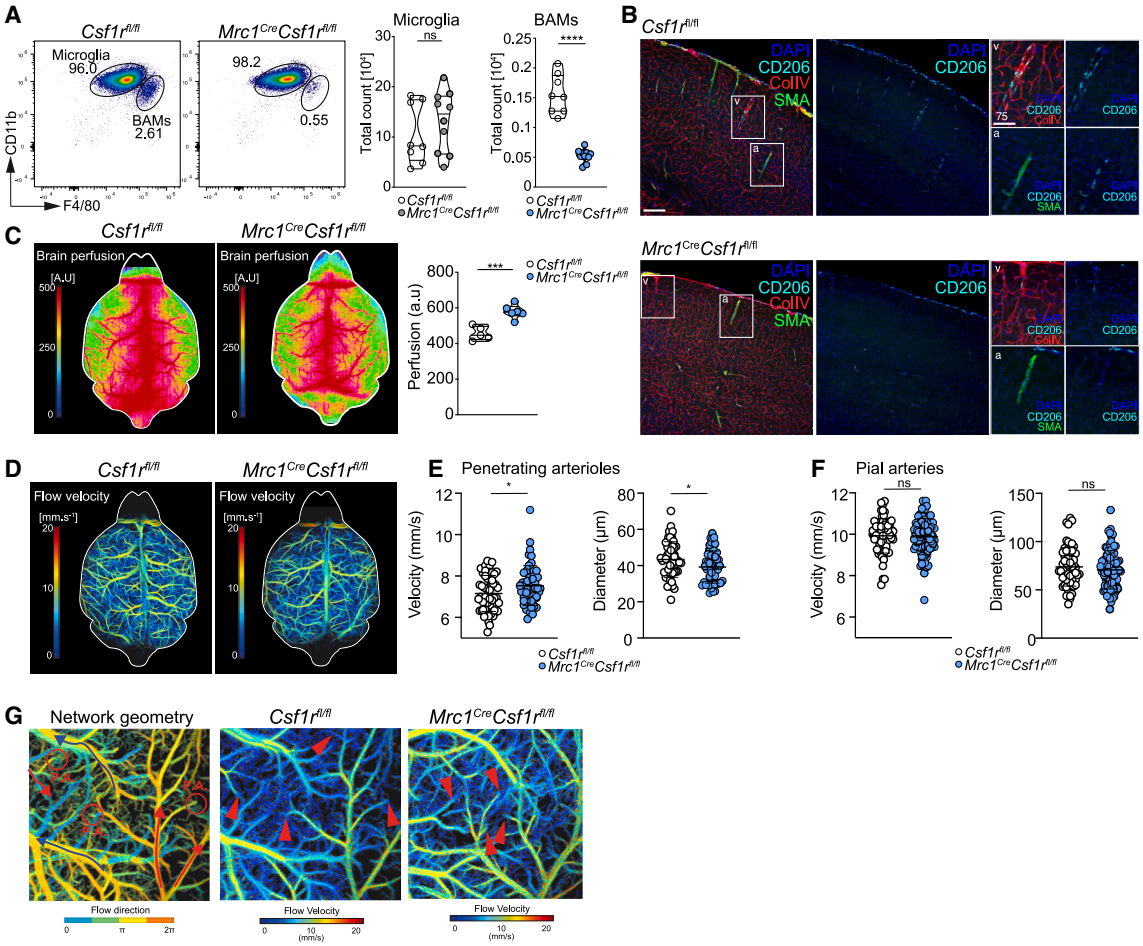

Figure 7. *Mrc1*^{Cre}*Csf1r*$^{fl/fl}$ mice display increased CBF

(A) Flow cytometry analysis of microglia and BAMs derived from brains of *Mrc1*^{Cre}*Csf1r*$^{fl/fl}$ and control (*Csf1r*$^{fl/fl}$ or *Mrc1*^{Cre}*Csf1r*$^{fl/+}$) mice (pregated on CD45$^+$Ly6C$^-$Ly6G$^-$CD64$^+$MerTK$^+$ cells). *n* = 8–10, pooled from 3 independent experiments.

(B) Immunofluorescence images of brain sections from *Csf1r*$^{fl/fl}$ and *Mrc1*^{Cre}*Csf1r*$^{fl/fl}$ mice stained for CD206 (cyan), ColIV (red), SMA (green), and DAPI (blue). Scale bar: 150 µm (insets 75 µm). *n* = 3, one experiment.

(C) Representative LSCI and graph tracing of brain perfusion in *Csf1r*$^{fl/fl}$ and *Mrc1*^{Cre}*Csf1r*$^{fl/fl}$ mice. *n* = 5–6, 1 experiment. 2 ROIs on each hemisphere per mouse were plotted.

(D) Representative Pia-FLOW intensity images showing blood flow velocity in the pial vessels of *Csf1r*$^{fl/fl}$ and *Mrc1*^{Cre}*Csf1r*$^{fl/fl}$ mice.

(E and F) Quantification of the basal blood flow velocity and vessel diameter in penetrating arterioles (E) and pial arteries (F). *n* = 5–6 from 1 experiment, *Csf1r*$^{fl/fl}$, 55 penetrating arterioles and 64 pial arteries; *Mrc1*^{Cre}*Csf1r*$^{fl/fl}$, 51 penetrating arterioles and 88 pial arteries.

(G) Representative Pia-FLOW image showing vascular network geometry identifying penetrating arterioles and flow direction (left). Penetrating arterioles are indicated in *Csf1r*$^{fl/fl}$ and *Mrc1*^{Cre}*Csf1r*$^{fl/fl}$ mice with red arrowheads.

Data are shown as mean and SD (E and F), data normality was performed using the D'Agostino & Pearson test. For normally distributed data, an unpaired Student's t test with Welch's correction was performed. Related to Figures S5–S7.

To assess whether reduction of CD206$^+$ BAMs also imprinted similar transcriptional changes in cells associated to the brain vasculature as in *Il34*-deficient mice, we performed scRNA-seq of sorted populations including fibroblasts, ECs, MCs, astrocytes, microglia, and BAMs derived from total brain cells (without the dura mater) of *Mrc1*^{Cre}*Csf1r*$^{fl/fl}$ and *Csf1r*$^{fl/fl}$ mice (Figures S7A and S7B). Altogether, the number of DEGs was highest in BAMs while ECs, astrocytes, and fibroblasts were not drastically changed (Figure S7C). Among BAMs, PVMs (*Cd163*$^+$, *Lyve1*$^+$, and *Mrc1*$^+$) and CD206$^+$MHC class II$^+$ BAMs (*Cd74*, *Ccr2*, and *H2-Ab1*) were detected, and the ratio between them was altered in *Mrc1*^{Cre}*Csf1r*$^{fl/fl}$ in favor of CD206$^+$MHC class II$^+$ BAMs (Figures S7D and S7E).

To explore whether common features can be found in CNS macrophages in the *Il34*$^{LacZ/LacZ}$ and the *Mrc1*^{Cre}*Csf1r*$^{fl/fl}$ scRNA-seq data, we integrated both datasets and used the combined controls (*Il34*$^{LacZ/+}$ and *Csf1r*$^{fl/fl}$) as reference. This comparison revealed that microglia were predominantly changed in the absence of *Il34*, while in *Mrc1*^{Cre}*Csf1r*$^{fl/fl}$ mice, BAMs displayed more differently expressed genes (Figures S7F and S7G). For example, microglia in *Il34*$^{LacZ/LacZ}$ mice downregulated signature genes including *P2ry12*, *Olfml3*, and *Tmem119*, and upregulated *Cd63* and *Ccl3* as previously described.[17] In the remaining BAMs, *Cd74*, *H2-Ab1*, *H2-Eb1*, and *H2-K1* were upregulated in both datasets, while *Pf4*,

Please cite this article in press as: Van Hove et al., Interleukin-34-dependent perivascular macrophages promote vascular function in the brain, Immunity (2025), https://doi.org/10.1016/j.immuni.2025.04.003

Cd163, and *Tyropb* were downregulated in the *Mrc1*^{Cre}*Csf1r*$^{fl/fl}$ BAMs compared with the combined control (Figure S7G). Similar changes in BAMs were described in neuroinflammation.[70]

To assess whether the increased blood flow velocity in *Il34*$^{LacZ/LacZ}$ mice is independent of microglia and instead results from the absence of PVMs, we analyzed *Mrc1*^{Cre}*Csf1r*$^{fl/fl}$ mice lacking PVMs. Similar to our observations in the *Il34*$^{LacZ/LacZ}$ mice, *Mrc1*^{Cre}*Csf1r*$^{fl/fl}$ mice showed increased blood perfusion, as assessed by LSCI (Figure 7C). We then assessed the CBF changes at vascular segments specifically focusing on penetrating pial arterioles where PVMs are localized. To address this, we examined changes in flow velocity and vessel diameters in relation to the local vascular network geometry using PiaFLOW imaging (Figures 7D–7G). This analysis demonstrates an increase in flow velocity in *Mrc1*^{Cre}*Csf1r*$^{fl/fl}$ mice, accompanied by a decrease in vessel diameters specifically at penetrating arterioles (Figures 7E and 7F), while pial arteries remained unaffected. Penetrating arterioles were identified as most distal arterial branches just before descending deeper into the brain (labeled with red arrows in Figure 7G). These findings indicate that altered vascular dynamics are confined to penetrating arterioles, demonstrating a critical role of PVMs in supporting vascular function.

DISCUSSION

We investigated the role of CSF-1R signaling in the development and survival of BAMs. CSF-1 was required for the embryonic development of all CNS macrophages but was mostly redundant for the homeostasis of BAMs at later postnatal phases. Conversely, even though IL-34 is already expressed in the developing brain,[19,43] it was not required for the accumulation and differentiation of CNS macrophages in embryogenesis or in the neonatal period. In adulthood, all BAM subsets (except those at the dura mater) were dependent on IL-34.

In *Il34*-deficient mice, transcriptional changes were observed across different cell types of the brain vasculature, which led to an altered cellular crosstalk. A previous *in vitro* study showed that IL-34 impacts the BBB by modulating tight junction proteins in CSF-1R^{+} ECs.[71] However, we did not detect *Csf1r* expression outside of macrophages and propose that the altered gene expression profile in vascular cells is an indirect effect of the reduced number of PVMs in the absence of IL-34. Furthermore, *Il34*-deficient mice did not exhibit a defective BBB, consistent with previous studies in mice lacking microglia and/or BAMs,[14,26,72–74] demonstrating that CNS macrophages are not required to maintain BBB permeability in healthy conditions.

In line with previous scRNA-seq data, we found that MCs and fibroblasts are also cellular sources of IL-34 in the brain, in addition to neurons.[18,19] Specifically deleting *Il34* in these cell types recapitulated the phenotype of reduced BAMs in *Il34*$^{LacZ/LacZ}$ mice, albeit to a lesser extent. This points to a role for mural- and perivascular fibroblast-derived IL-34 in the maintenance of PVMs. It was recently demonstrated that PVM development is impaired in Notch3$^{-/-}$ mice, in which VSMCs are reduced and display an altered phenotype,[41] supporting the possibility that VSMCs provide a survival signal for PVMs. We demonstrate that IL-34 is such a survival signal. Our data showing the expression of IL-34 at the human vasculature are supported by recent scRNA-seq data.[46] A recent report showed that IL-34 in the serum was decreased in patients with vascular dementia, a condition associated with impaired CBF, and this correlated with cognitive impairment.[75] These results suggest that the role we observed for IL-34 in the regulation of mouse CNS macrophages may also exist in humans.

Loss of *Il34* resulted in increased CBF compared with controls, consistent with recent findings in mice eliminated of all CSF-1R-dependent macrophages, including CNS macrophages.[76] Similarly, *Mrc1*^{Cre}*Csf1r*$^{fl/fl}$ mice exhibited increased CBF and perfusion, pointing toward an important role specifically of PVMs in cerebral vascular regulation. Notably, vasomotion, typically observed in arterioles, was also elevated in the absence of IL-34. While vasomotion has been shown to contribute to paravascular clearance of brain solutes,[77] the underlying mechanisms remain unclear. Here, we show that IL-34/PVMs play a role in the regulation of vasomotion. Taken together, these findings strongly support a critical and specific role for PVMs in maintaining vascular dynamics at cerebral arterioles and pial arteries.

In summary, we demonstrate a niche-specific signaling at brain blood vessels, showing that murine BAMs require mural cell- and perivascular fibroblast-derived IL-34 for their homeostasis in the adult brain. Additionally, we identified a critical function for PVMs in regulating cerebral vascular dynamics.

Limitations of the study

A recent study demonstrated that *Il34* deficiency has no overall effect on neurons or glia.[78] Yet, the possibility that IL-34 has additional roles, such as acting on the PTPRZ1 expressed by neurons and astrocytes, cannot be excluded. The increased GFAP staining observed along arterioles in *Il34*$^{LacZ/LacZ}$ mice suggests astrocyte reactivity,[64] which may further contribute to vascular dysfunction.

In addition to PVMs, microglia are also drastically reduced in *Il34*-deficient mice and display an altered gene expression profile, including downregulation of homeostatic genes such as *P2ry12*,[17] that has recently been implicated in the regulation of capillary structure, vasodilation, and blood flow.[76,79] One potential consideration is that capillary-associated microglia may also be impaired in these mice, impacting their support of capillary structure and function, and thereby contributing to the impaired hemodynamics in the absence of IL-34. However, *Il34*$^{LacZ/LacZ}$ mice display elevated blood flow velocity in the main leptomeningeal arterioles, where PVMs are present. This was also observed in *Mrc1*^{Cre}*Csf1r*$^{fl/fl}$ mice, where specifically PVMs were absent while microglia remained present, indicating that PVMs promote cerebrovascular function independently of microglial contributions.

Our study uncovers a role for CNS macrophages in regulating vascular function and shaping the blood flow dynamics, particularly in arterioles. Future studies investigating how chronic increases in blood flow in arterioles lacking PVMs lead to long-term vascular dysfunction would be interesting for understanding how these findings may translate to disease conditions.

Finally, while we identified a crosstalk between the vasculature and PVMs, the signals by PVMs for vascular cells remain to be identified.

RESOURCE AVAILABILITY

Lead contact

Further information and requests for resources and reagents should be directed to and will be fulfilled by the lead contact, Melanie Greter (greter@immunology.uzh.ch).

Materials availability

All unique/stable reagents generated in this study are available from the lead contact.

Data and code availability

The scRNA-seq data have been deposited in GEO (GEO: GSE292245, GSE292306, and GSE292466) and are publicly available as of the date of publication. The accession is listed in the key resources table. This paper does not report original code. Any additional information required to reanalyze the data reported in this paper is available from the lead contact upon request.

ACKNOWLEDGMENTS

This work was supported by grants from the Swiss National Science Foundation (310030_184915, PP00P3_170626, and BSSGI0_155832 to M.G.; 31003A_159514, 310030_188952, 320030_228518 to A.K.; PP00P3_202663 to S.W.; 310030_182703 to B.W., 733 310030_170320, 310030_188450, and CRSII5_183478 to B.B.; and Ambizione PZ00P3-193330 to S.M.), the Medical Research Center the Loop to B.B., the Swiss Cancer League (grant KLS-3848-02-2016 to B.B. and KFS-5533-02-2022 to M.G.), the Synapsis Foundation and the Choupette Foundation (grant 2019-PI02) to A.K., the Swiss Heart Foundation to M.E.A., ERA-NET NEURON (32NE30_213467) to A.K., and UZH Postdoc Grant (FK-24-048) to C.G. This project has received funding from the European Research Council (ERC) under the European Union's Horizon 2020 research and innovation program (grant agreement no. 819229 to M.G.) and a US NIH grant (AG045040) and Welch Foundation grant (AQ-1507) to J.X.J.

We thank the Flow Cytometry Facility (University of Zurich), the Center for Microscopy and Image Analysis (University of Zurich), and Dr. Doris Popovic as well as Daymé González Rodríguez from the Functional Genomics Center (University of Zurich) for technical support. We would also like to thank Mirjam Lutz, André Fonseca Da Silva, and Nicole Puertas for their technical support. J. X.J. provided the *Csf1*$^{fl/fl}$ mice. We also wish to thank Dr. Daniel Ackerman from Insight Editing London for assistance in reviewing the manuscript.

AUTHOR CONTRIBUTIONS

Conceptualization, M.G., A.K., W.M., M.E.A., C.G., and H.V.H.; methodology, H.V.H., W.M., C.G., E.P., M.E.A., A.K., U.M., S.W., B.W., and C.S.; investigation, W.M., E.P., M.V., U.M., P.H., C.M., C.G., S.G.U., H.V.H., V.K., J.D., F.I., C. A., E.R., S.A.S., I.L., S.-F.H., Q.Z., Z.C., C.C., S.B., J.S., D.R., and A.K.; resources, J.X.J., K.A., P.P., and E.P.; software, F.I. and V.K.; writing, W.M., C.G., H.V.H, M.E.A., and M.G.; review & editing, C.S., B.W., S.W., S.T., M.E. A., A.K., B.B., and M.G.; funding acquisition, A.K., B.B., M.G., S.W., M.E.A., and B.W.

DECLARATION OF INTERESTS

The authors declare no competing interests.

STAR★METHODS

Detailed methods are provided in the online version of this paper and include the following:

SUPPLEMENTAL INFORMATION

Supplemental information can be found online at https://doi.org/10.1016/j.immuni.2025.04.003.

Received: January 21, 2025
Revised: March 21, 2025
Accepted: April 3, 2025
Published: May 1, 2025

REFERENCES

1. Mildenberger, W., Stifter, S.A., and Greter, M. (2022). Diversity and function of brain-associated macrophages. Curr. Opin. Immunol. *76*, 102181. https://doi.org/10.1016/j.coi.2022.102181.
2. Prinz, M., Masuda, T., Wheeler, M.A., and Quintana, F.J. (2021). Microglia and Central Nervous System–Associated Macrophages—From Origin to Disease Modulation. Annu. Rev. Immunol. *39*, 251–277. https://doi.org/10.1146/annurev-immunol-093019-110159.
3. Ginhoux, F., Greter, M., Leboeuf, M., Nandi, S., See, P., Gokhan, S., Mehler, M.F., Conway, S.J., Ng, L.G., Stanley, E.R., et al. (2010). Fate mapping analysis reveals that adult microglia derive from primitive macrophages. Science *330*, 841–845. https://doi.org/10.1126/science.1194637.
4. Schulz, C., Perdiguero, E.G., Chorro, L., Szabo-Rogers, H., Cagnard, N., Kierdorf, K., Prinz, M., Wu, B., Jacobsen, S.E.W., Pollard, J.W., et al. (2012). A lineage of myeloid cells independent of myb and hematopoietic stem cells. Science *336*, 86–90. https://doi.org/10.1126/science.1219179.
5. Goldmann, T., Wieghofer, P., Jordão, M.J.C., Prutek, F., Hagemeyer, N., Frenzel, K., Amann, L., Staszewski, O., Kierdorf, K., Krueger, M., et al. (2016). Origin, fate and dynamics of macrophages at central nervous system interfaces. Nat. Immunol. *17*, 797–805. https://doi.org/10.1038/ni.3423.
6. Kierdorf, K., Erny, D., Goldmann, T., Sander, V., Schulz, C., Perdiguero, E. G., Wieghofer, P., Heinrich, A., Riemke, P., Hölscher, C., et al. (2013). Microglia emerge from erythromyeloid precursors via Pu.1-and Irf8-dependent pathways. Nat. Neurosci. *16*, 273–280. https://doi.org/10.1038/nn.3318.

7. Van Hove, H., Martens, L., Scheyltjens, I., De Vlaminck, K., Pombo Antunes, A.R., De Prijck, S., Vandamme, N., De Schepper, S., Van Isterdael, G., Scott, C.L., et al. (2019). A single-cell atlas of mouse brain macrophages reveals unique transcriptional identities shaped by ontogeny and tissue environment. Nat. Neurosci. *22*, 1021–1035. https://doi.org/10.1038/s41593-019-0393-4.

8. Mrdjen, D., Pavlovic, A., Hartmann, F.J., Schreiner, B., Utz, S.G., Leung, B. P., Lelios, I., Heppner, F.L., Kipnis, J., Merkler, D., et al. (2018). High-Dimensional Single-Cell Mapping of Central Nervous System Immune Cells Reveals Distinct Myeloid Subsets in Health, Aging, and Disease. Immunity *48*, 380–395.e6. https://doi.org/10.1016/j.immuni.2018.01.011.

9. Karam, M., Janbon, H., Malkinson, G., and Brunet, I. (2022). Heterogeneity and developmental dynamics of LYVE-1 perivascular macrophages distribution in the mouse brain. J. Cereb. Blood Flow Metab. *42*, 1797–1812. https://doi.org/10.1177/0271678X221101643.

10. Faraco, G., Park, L., Anrather, J., and Iadecola, C. (2017). Brain perivascular macrophages: characterization and functional roles in health and disease. J. Mol. Med. (Berl) *95*, 1143–1152. https://doi.org/10.1007/s00109-017-1573-x.

11. Borst, K., Dumas, A.A., and Prinz, M. (2021). Microglia: Immune and non-immune functions. Immunity *54*, 2194–2208. https://doi.org/10.1016/j.immuni.2021.09.014.

12. Rojo, R., Raper, A., Ozdemir, D.D., Lefevre, L., Grabert, K., Wollscheid-Lengeling, E., Bradford, B., Caruso, M., Gazova, I., Sánchez, A., et al. (2019). Deletion of a Csf1r enhancer selectively impacts CSF1R expression and development of tissue macrophage populations. Nat. Commun. *10*, 3215. https://doi.org/10.1038/s41467-019-11053-8.

13. Buttgereit, A., Lelios, I., Yu, X., Vrohlings, M., Krakoski, N.R., Gautier, E.L., Nishinakamura, R., Becher, B., and Greter, M. (2016). Sall1 is a transcriptional regulator defining microglia identity and function. Nat. Immunol. *17*, 1397–1406. https://doi.org/10.1038/ni.3585.

14. Elmore, M.R.P., Najafi, A.R., Koike, M.A., Dagher, N.N., Spangenberg, E. E., Rice, R.A., Kitazawa, M., Matusow, B., Nguyen, H., West, B.L., et al. (2014). Colony-stimulating factor 1 receptor signaling is necessary for microglia viability, unmasking a microglia progenitor cell in the adult brain. Neuron *82*, 380–397. https://doi.org/10.1016/j.neuron.2014.02.040.

15. Wiktor-Jedrzejczak, W., Bartocci, A., Ferrante, A.W., Ahmed-Ansari, A., Sell, K.W., Pollard, J.W., and Stanley, E.R. (1990). Total absence of colony-stimulating factor 1 in the macrophage-deficient osteopetrotic (op/op) mouse. Proc. Natl. Acad. Sci. USA *87*, 4828–4832. https://doi.org/10.1073/pnas.87.12.4828.

16. Lin, H., Lee, E., Hestir, K., Leo, C., Huang, M., Bosch, E., Halenbeck, R., Wu, G., Zhou, A., Behrens, D., et al. (2008). Discovery of a cytokine and its receptor by functional screening of the extracellular proteome. Science *320*, 807–811. https://doi.org/10.1126/science.1154370.

17. Kana, V., Desland, F.A., Casanova-Acebes, M., Ayata, P., Badimon, A., Nabel, E., Yamamuro, K., Sneeboer, M., Tan, I.L., Flanigan, M.E., et al. (2019). CSF-1 controls cerebellar microglia and is required for motor function and social interaction. J. Exp. Med. *216*, 2265–2281. https://doi.org/10.1084/jem.20182037.

18. Wang, Y., Szretter, K.J., Vermi, W., Gilfillan, S., Rossini, C., Cella, M., Barrow, A.D., Diamond, M.S., and Colonna, M. (2012). IL-34 is a tissue-restricted ligand of CSF1R required for the development of Langerhans cells and microglia. Nat. Immunol. *13*, 753–760. https://doi.org/10.1038/ni.2360.

19. Greter, M., Lelios, I., Pelczar, P., Hoeffel, G., Price, J., Leboeuf, M., Kündig, T.M., Frei, K., Ginhoux, F., Merad, M., et al. (2012). Stroma-Derived Interleukin-34 Controls the Development and Maintenance of Langerhans Cells and the Maintenance of Microglia. Immunity *37*, 1050–1060. https://doi.org/10.1016/j.immuni.2012.11.001.

20. Wolf, S.A., Boddeke, H.W.G.M., and Kettenmann, H. (2017). Microglia in Physiology and Disease. Annu. Rev. Physiol. *79*, 619–643. https://doi.org/10.1146/annurev-physiol-022516-034406.

21. Rebejac, J., Eme-Scolan, E., Arnaud Paroutaud, L., Kharbouche, S., Teleman, M., Spinelli, L., Gallo, E., Roussel-Queval, A., Zarubica, A., Sansoni, A., et al. (2022). Meningeal macrophages protect against viral neuroinfection. Immunity *55*, 2103–2117.e10. https://doi.org/10.1016/J.IMMUNI.2022.10.005.

22. De Vlaminck, K., Van Hove, H., Kancheva, D., Scheyltjens, I., Pombo Antunes, A.R., Bastos, J., Vara-Perez, M., Ali, L., Mampay, M., Deneyer, L., et al. (2022). Differential plasticity and fate of brain-resident and recruited macrophages during the onset and resolution of neuroinflammation. Immunity *55*, 2085–2102.e9. https://doi.org/10.1016/J.IMMUNI.2022.09.005.

23. Hawkes, C.A., and McLaurin, J. (2009). Selective targeting of perivascular macrophages for clearance of β-amyloid in cerebral amyloid angiopathy. Proc. Natl. Acad. Sci. USA *106*, 1261–1266. https://doi.org/10.1073/pnas.0805453106.

24. Bijnen, M., Sridhar, S., Keller, A., and Greter, M. (2025). Brain macrophages in vascular health and dysfunction. Trends Immunol. *46*, 46–60. https://doi.org/10.1016/j.it.2024.11.012.

25. Pires, P.W., Girgla, S.S., Mcclain, J.L., Kaminski, N.E., van Rooijen, N., and Dorrance, A.M. (2013). Improvement in middle cerebral artery structure and endothelial function in stroke-prone spontaneously hypertensive rats after macrophage depletion. Microcirculation *20*, 650–661. https://doi.org/10.1111/micc.12064.

26. Santisteban, M.M., Ahn, S.J., Lane, D., Faraco, G., Garcia-Bonilla, L., Racchumi, G., Poon, C., Schaeffer, S., Segarra, S.G., Körbelin, J., et al. (2020). Endothelium-Macrophage Crosstalk Mediates Blood-Brain Barrier Dysfunction in Hypertension. Hypertension *76*, 795–807. https://doi.org/10.1161/HYPERTENSIONAHA.120.15581.

27. Santisteban, M.M., Schaeffer, S., Anfray, A., Faraco, G., Brea, D., Wang, G., Sobanko, M.J., Sciortino, R., Racchumi, G., Waisman, A., et al. (2024). Meningeal interleukin-17-producing T cells mediate cognitive impairment in a mouse model of salt-sensitive hypertension. Nat. Neurosci. *27*, 63–77. https://doi.org/10.1038/s41593-023-01497-z.

28. Park, L., Uekawa, K., Garcia-Bonilla, L., Koizumi, K., Murphy, M., Pistik, R., Younkin, L., Younkin, S., Zhou, P., Carlson, G., et al. (2017). Brain Perivascular Macrophages Initiate the Neurovascular Dysfunction of Alzheimer Aβ Peptides. Circ. Res. *121*, 258–269. https://doi.org/10.1161/CIRCRESAHA.117.311054.

29. Iadecola, C., Anfray, A., Schaeffer, S., Hattori, Y., Santisteban, M., Casey, N., Wang, G., Strickland, M., Zhou, P., Holtzman, D., et al. (2023). Cell autonomous role of border associated macrophages in ApoE4 neurovascular dysfunction and susceptibility to white matter injury. Res Sq, rs.3.rs-3222611. https://doi.org/10.21203/rs.3.rs-3222611/v1.

30. Pedragosa, J., Salas-Perdomo, A., Gallizioli, M., Cugota, R., Miró-Mur, F., Briansó, F., Justicia, C., Pérez-Asensio, F., Marquez-Kisinousky, L., Urra, X., et al. (2018). CNS-border associated macrophages respond to acute ischemic stroke attracting granulocytes and promoting vascular leakage. Acta Neuropathol. Commun. *6*, 76. https://doi.org/10.1186/s40478-018-0581-6.

31. Drieu, A., Du, S., Storck, S.E., Rustenhoven, J., Papadopoulos, Z., Dykstra, T., Zhong, F., Kim, K., Blackburn, S., Mamuladze, T., et al. (2022). Parenchymal border macrophages regulate the flow dynamics of the cerebrospinal fluid. Nature *7936*, 585–593. https://doi.org/10.1038/s41586-022-05397-3.

32. Schaffenrath, J., and Keller, A. (2020). New Insights in the Complexity and Functionality of the Neurovascular Unit. In Physiology, Pharmacology and Pathology of the Blood-Brain Barrier. Handbook of Experimental Pharmacology, Z. Cader and W. Neuhaus, eds. (Springer). https://doi.org/10.1007/164_2020_424.

33. Iadecola, C. (2017). The Neurovascular Unit Coming of Age: A Journey through Neurovascular Coupling in Health and Disease. Neuron *96*, 17–42. https://doi.org/10.1016/j.neuron.2017.07.030.

34. Mastorakos, P., and McGavern, D. (2019). The anatomy and immunology of vasculature in the central nervous system. Sci. Immunol. *4*, eaav0492. https://doi.org/10.1126/SCIIMMUNOL.AAV0492.

35. Sweeney, M.D., Zhao, Z., Montagne, A., Nelson, A.R., and Zlokovic, B.V. (2019). Blood-Brain Barrier: From Physiology to Disease and Back. Physiol. Rev. *99*, 21–78. https://doi.org/10.1152/physrev.00050.2017.

36. Mateo, C., Knutsen, P.M., Tsai, P.S., Shih, A.Y., and Kleinfeld, D. (2017). Entrainment of Arteriole Vasomotor Fluctuations by Neural Activity Is a Basis of Blood-Oxygenation-Level-Dependent "Resting-State" Connectivity. Neuron *96*, 936–948.e3. https://doi.org/10.1016/j.neuron.2017.10.012.

37. Broggini, T., Duckworth, J., Ji, X., Liu, R., Xia, X., Mächler, P., Shaked, I., Munting, L.P., Iyengar, S., Kotlikoff, M., et al. (2024). Long-wavelength traveling waves of vasomotion modulate the perfusion of cortex. Neuron *112*, 2349–2367.e8. https://doi.org/10.1016/j.neuron.2024.04.034.

38. Utz, S.G., See, P., Mildenberger, W., Thion, M.S., Silvin, A., Lutz, M., Ingelfinger, F., Rayan, N.A., Lelios, I., Buttgereit, A., et al. (2020). Early Fate Defines Microglia and Non-parenchymal Brain Macrophage Development. Cell *181*, 557–573.e18. https://doi.org/10.1016/j.cell.2020.03.021.

39. Mass, E., Ballesteros, I., Farlik, M., Halbritter, F., Günther, P., Crozet, L., Jacome-Galarza, C.E., Händler, K., Klughammer, J., Kobayashi, Y., et al. (2016). Specification of tissue-resident macrophages during organogenesis. Science *353*, aaf4238. https://doi.org/10.1126/science.aaf4238.

40. Hattori, Y., Kato, D., Murayama, F., Koike, S., Asai, H., Yamasaki, A., Naito, Y., Kawaguchi, A., Konishi, H., Prinz, M., et al. (2023). CD206+ macrophages transventricularly infiltrate the early embryonic cerebral wall to differentiate into microglia. Cell Rep. *42*, 112092. https://doi.org/10.1016/j.celrep.2023.112092.

41. Masuda, T., Amann, L., Monaco, G., Sankowski, R., Staszewski, O., Krueger, M., Del Gaudio, F., He, L., Paterson, N., Nent, E., et al. (2022). Specification of CNS macrophage subsets occurs postnatally in defined niches. Nature *604*, 740–748. https://doi.org/10.1038/s41586-022-04596-2.

42. Dai, X.M., Ryan, G.R., Hapel, A.J., Dominguez, M.G., Russell, R.G., Kapp, S., Sylvestre, V., and Stanley, E.R. (2002). Targeted disruption of the mouse colony-stimulating factor 1 receptor gene results in osteopetrosis, mononuclear phagocyte deficiency, increased primitive progenitor cell frequencies, and reproductive defects. Blood *99*, 111–120. https://doi.org/10.1182/blood.V99.1.111.

43. Nandi, S., Gokhan, S., Dai, X.M., Wei, S., Enikolopov, G., Lin, H., Mehler, M.F., and Stanley, E.R. (2012). The CSF-1 receptor ligands IL-34 and CSF-1 exhibit distinct developmental brain expression patterns and regulate neural progenitor cell maintenance and maturation. Dev. Biol. *367*, 100–113. https://doi.org/10.1016/j.ydbio.2012.03.026.

44. Munro, D.A.D., Movahedi, K., and Priller, J. (2022). Macrophage compartmentalization in the brain and cerebrospinal fluid system. Sci. Immunol. *7*, eabk0391. https://doi.org/10.1126/sciimmunol.abk0391.

45. Vanlandewijck, M., He, L., Mäe, M.A., Andrae, J., Ando, K., Del Gaudio, F., Nahar, K., Lebouvier, T., Laviña, B., Gouveia, L., et al. (2018). A molecular atlas of cell types and zonation in the brain vasculature. Nature *554*, 475–480. https://doi.org/10.1038/nature25739.

46. Yang, A.C., Vest, R.T., Kern, F., Lee, D.P., Agam, M., Maat, C.A., Losada, P.M., Chen, M.B., Schaum, N., Khoury, N., et al. (2022). A human brain vascular atlas reveals diverse mediators of Alzheimer's risk. Nature *603*, 885–892. https://doi.org/10.1038/s41586-021-04369-3.

47. Nandi, S., Cioce, M., Yeung, Y.G., Nieves, E., Tesfa, L., Lin, H., Hsu, A.W., Halenbeck, R., Cheng, H.Y., Gokhan, S., et al. (2013). Receptor-type protein-tyrosine phosphatase ζ is a functional receptor for interleukin-34. J. Biol. Chem. *288*, 21972–21986. https://doi.org/10.1074/jbc.M112.442731.

48. Guimarães-Camboa, N., Cattaneo, P., Sun, Y., Moore-Morris, T., Gu, Y., Dalton, N.D., Rockenstein, E., Masliah, E., Peterson, K.L., Stallcup, W.B., et al. (2017). Pericytes of Multiple Organs Do Not Behave as Mesenchymal Stem Cells In Vivo. Cell Stem Cell *20*, 345–359.e5. https://doi.org/10.1016/J.STEM.2016.12.006.

49. Zeisel, A., Moz-Manchado, A.B., Codeluppi, S., Lönnerberg, P., Manno, G.L., Juréus, A., Marques, S., Munguba, H., He, L., Betsholtz, C., et al. (2015). Cell types in the mouse cortex and hippocampus revealed by single-cell RNA-seq. Science *347*, 1138–1142. https://doi.org/10.1126/science.aaa1934.

50. Hume, D.A., Caruso, M., Ferrari-Cestari, M., Summers, K.M., Pridans, C., and Irvine, K.M. (2020). Phenotypic impacts of CSF1R deficiencies in humans and model organisms. J. Leukoc. Biol. *107*, 205–219. https://doi.org/10.1002/JLB.MR0519-143R.

51. Shintani, T., Watanabe, E., Maeda, N., and Noda, M. (1998). Neurons as well as astrocytes express proteoglycan-type protein tyrosine phosphatase ζ/RPTPβ: Analysis of mice in which the PTPζ/RPTPβ gene was replaced with the LacZ gene. Neurosci. Lett. *247*, 135–138. https://doi.org/10.1016/S0304-3940(98)00295-X.

52. Von Holst, A., Sirko, S., and Faissner, A. (2006). The unique 473HD-chondroitinsulfate epitope is expressed by radial glia and involved in neural precursor cell proliferation. J. Neurosci. *26*, 4082–4094. https://doi.org/10.1523/JNEUROSCI.0422-06.2006.

53. Segaliny, A.I., Brion, R., Mortier, E., Maillasson, M., Cherel, M., Jacques, Y., Le Goff, B., and Heymann, D. (2015). Syndecan-1 regulates the biological activities of interleukin-34. Biochim. Biophys. Acta *1853*, 1010–1021. https://doi.org/10.1016/j.bbamcr.2015.01.023.

54. Dong, X., Tan, N.B., Howell, K.B., Barresi, S., Freeman, J.L., Vecchio, D., Piccione, M., Radio, F.C., Calame, D., Zong, S., et al. (2020). Bi-allelic LoF NRROS Variants Impairing Active TGF-β1 Delivery Cause a Severe Infantile-Onset Neurodegenerative Condition with Intracranial Calcification. Am. J. Hum. Genet. *106*, 559–569. https://doi.org/10.1016/J.AJHG.2020.02.014.

55. Jin, S., Guerrero-Juarez, C.F., Zhang, L., Chang, I., Ramos, R., Kuan, C.H., Myung, P., Plikus, M.V., and Nie, Q. (2021). Inference and analysis of cell-cell communication using CellChat. Nat. Commun. *12*, 1088. https://doi.org/10.1038/s41467-021-21246-9.

56. Von Der Thüsen, J.H., Borensztajn, K.S., Moimas, S., Van Heiningen, S., Teeling, P., Van Berkel, T.J.C., and Biessen, E.A.L. (2011). IGF-1 has plaque-stabilizing effects in atherosclerosis by altering vascular smooth muscle cell phenotype. Am. J. Pathol. *178*, 924–934. https://doi.org/10.1016/j.ajpath.2010.10.007.

57. Miller, L.R., Bickel, M.A., Tarantini, S., Runion, M.E., Matacchiera, Z., Vance, M.L., Hibbs, C., Vaden, H., Nagykaldi, D., Martin, T., et al. (2024). IGF1R deficiency in vascular smooth muscle cells impairs myogenic autoregulation and cognition in mice. Front. Aging Neurosci. *16*, 1320808. https://doi.org/10.3389/fnagi.2024.1320808.

58. Sun, Y., Jin, K., Childs, J.T., Xie, L., Mao, X.O., and Greenberg, D.A. (2004). Increased severity of cerebral ischemic injury in vascular endothelial growth factor-B-deficient mice. J. Cereb. Blood Flow Metab. *24*, 1146–1152. https://doi.org/10.1097/01.WCB.0000134477.38980.38.

59. Silvestre, J.-S., Tamarat, R., Ebrahimian, T.G., Le-Roux, A., Clergue, M., Emmanuel, F., Duriez, M., Schwartz, B., Branellec, D., and Lévy, B.I. (2003). Vascular endothelial growth factor-B promotes in vivo angiogenesis. Circ. Res. *93*, 114–123. https://doi.org/10.1161/01.RES.0000081594.21764.44.

60. Henshall, T.L., Keller, A., He, L., Johansson, B.R., Wallgard, E., Raschperger, E., Mäe, M.A., Jin, S., Betsholtz, C., and Lendahl, U. (2015). Notch3 is necessary for blood vessel integrity in the central nervous system. Arterioscler. Thromb. Vasc. Biol. *35*, 409–420. https://doi.org/10.1161/ATVBAHA.114.304849.

61. Armulik, A., Genové, G., Mäe, M., Nisancioglu, M.H., Wallgard, E., Niaudet, C., He, L., Norlin, J., Lindblom, P., Strittmatter, K., et al. (2010). Pericytes regulate the blood-brain barrier. Nature *468*, 557–561. https://doi.org/10.1038/nature09522.

62. Brindle, N.P.J., Saharinen, P., and Alitalo, K. (2006). Signaling and functions of angiopoietin-1 in vascular protection. Circ. Res. *98*, 1014–1023. https://doi.org/10.1161/01.RES.0000218275.54089.12.

63. Xia, H., and Lazartigues, E. (2008). Angiotensin-converting enzyme 2 in the brain: properties and future directions. J. Neurochem. *107*, 1482–1494. https://doi.org/10.1111/J.1471-4159.2008.05723.X.

64. Linnerbauer, M., Wheeler, M.A., and Quintana, F.J. (2020). Astrocyte Crosstalk in CNS Inflammation. Neuron *108*, 608–622. https://doi.org/10.1016/j.neuron.2020.08.012.

65. Salman, M.M., Kitchen, P., Halsey, A., Wang, M.X., Törnroth-Horsefield, S., Conner, A.C., Badaut, J., Iliff, J.J., and Bill, R.M. (2022). Emerging roles for dynamic aquaporin-4 subcellular relocalization in CNS water homeostasis. Brain *145*, 64–75. https://doi.org/10.1093/brain/awab311.

66. Glück, C., Zhou, Q., Droux, J., Chen, Z., Glandorf, L., Wegener, S., Razansky, D., Weber, B., and El Amki, M.E. (2024). Pia-FLOW: Deciphering hemodynamic maps of the pial vascular connectome and its response to arterial occlusion. Proc. Natl. Acad. Sci. USA *121*, e2402624121. https://doi.org/10.1073/pnas.2402624121.

67. Silverman, A., and Petersen, N.H. (2025). Physiology, Cerebral Autoregulation. In StatPearls (StatPearls Publishing).

68. Faraco, G., Sugiyama, Y., Lane, D., Garcia-Bonilla, L., Chang, H., Santisteban, M.M., Racchumi, G., Murphy, M., Van Rooijen, N., Anrather, J., et al. (2016). Perivascular macrophages mediate the neurovascular and cognitive dysfunction associated with hypertension. J. Clin. Invest. *126*, 4674–4689. https://doi.org/10.1172/JCI86950.

69. Hauglund, N.L., Andersen, M., Tokarska, K., Radovanovic, T., Kjaerby, C., Sørensen, F.L., Bojarowska, Z., Untiet, V., Ballestero, S.B., Kolmos, M.G., et al. (2025). Norepinephrine-mediated slow vasomotion drives glymphatic clearance during sleep. Cell *188*, 606–622.e17. https://doi.org/10.1016/j.cell.2024.11.027.

70. Jordão, M.J.C., Sankowski, R., Brendecke, S.M., Sagar, Locatelli, G., Tai, Y.H., Tay, T.L., Schramm, E., Armbruster, S., Hagemeyer, N., et al. (2019). Single-cell profiling identifies myeloid cell subsets with distinct fates during neuroinflammation. Science *363*, eaat7554. https://doi.org/10.1126/science.aat7554.

71. Jin, S., Sonobe, Y., Kawanokuchi, J., Horiuchi, H., Cheng, Y., Wang, Y., Mizuno, T., Takeuchi, H., and Suzumura, A. (2014). Interleukin-34 Restores Blood–Brain Barrier Integrity by Upregulating Tight Junction Proteins in Endothelial Cells. PLoS One *9*, e115981. https://doi.org/10.1371/JOURNAL.PONE.0115981.

72. Profaci, C.P., Harvey, S.S., Bajc, K., Zhang, T.Z., Jeffrey, D.A., Zhang, A. Z., Nemec, K.M., Davtyan, H., O'Brien, C.A., McKinsey, G.L., et al. (2024). Microglia are not necessary for maintenance of blood-brain barrier properties in health, but PLX5622 alters brain endothelial cholesterol metabolism. Neuron *112*, 2910–2921.e7. https://doi.org/10.1016/j.neuron.2024.07.015.

73. Kerkhofs, D., Van Hagen, B.T., Milanova, I.V., Schell, K.J., Van Essen, H., Wijnands, E., Goossens, P., Blankesteijn, W.M., Unger, T., Prickaerts, J., et al. (2020). Pharmacological depletion of microglia and perivascular macrophages prevents Vascular Cognitive Impairment in Ang II-induced hypertension. Theranostics *10*, 9512–9527. https://doi.org/10.7150/thno.44394.

74. Munro, D.A.D., Bestard-Cuche, N., McQuaid, C., Chagnot, A., Shabestari, S.K., Chadarevian, J.P., Maheshwari, U., Szymkowiak, S., Morris, K., Mohammad, M., et al. (2024). Microglia protect against age-associated brain pathologies. Neuron *112*, 2732–2748.e8. https://doi.org/10.1016/j.neuron.2024.05.018.

75. Wang, Y., Lu, W., Ning, W., Chen, Y., and Li, L. (2021). Decreased Levels of Serum IL-34 Associated with Cognitive Impairment in Vascular Dementia. BioMed Res. Int. *2021*, 6793860. https://doi.org/10.1155/2021/6793860.

76. Császár, E., Lénárt, N., Cserép, C., Környei, Z., Fekete, R., Pósfai, B., Balázsfi, D., Hangya, B., Schwarcz, A.D., Szabadits, E., et al. (2022). Microglia modulate blood flow, neurovascular coupling, and hypoperfusion via purinergic actions. J. Exp. Med. *219*, e20211071. https://doi.org/10.1084/jem.20211071.

77. van Veluw, S.J., Hou, S.S., Calvo-Rodriguez, M., Arbel-Ornath, M., Snyder, A.C., Frosch, M.P., Greenberg, S.M., and Bacskai, B.J. (2020). Vasomotion as a Driving Force for Paravascular Clearance in the Awake Mouse Brain. Neuron *105*, 549–561.e5. https://doi.org/10.1016/j.neuron.2019.10.033.

78. Badimon, A., Strasburger, H.J., Ayata, P., Chen, X., Nair, A., Ikegami, A., Hwang, P., Chan, A.T., Graves, S.M., Uweru, J.O., et al. (2020). Negative feedback control of neuronal activity by microglia. Nature *586*, 417–423. https://doi.org/10.1038/s41586-020-2777-8.

79. Bisht, K., Okojie, K.A., Sharma, K., Lentferink, D.H., Sun, Y.Y., Chen, H.R., Uweru, J.O., Amancherla, S., Calcuttawala, Z., Campos-Salazar, A.B., et al. (2021). Capillary-associated microglia regulate vascular structure and function through PANX1-P2RY12 coupling in mice. Nat. Commun. *12*, 5289. https://doi.org/10.1038/s41467-021-25590-8.

80. Becht, E., McInnes, L., Healy, J., Dutertre, C.A., Kwok, I.W.H., Ng, L.G., Ginhoux, F., and Newell, E.W. (2019). Dimensionality reduction for visualizing single-cell data using UMAP. Nat. Biotechnol. *37*, 38–44. https://doi.org/10.1038/nbt.4314.

81. Van Gassen, S., Callebaut, B., Van Helden, M.J., Lambrecht, B.N., Demeester, P., Dhaene, T., and Saeys, Y. (2015). FlowSOM: Using self-organizing maps for visualization and interpretation of cytometry data. Cytometry A *87*, 636–645. https://doi.org/10.1002/CYTO.A.22625.

82. Schindelin, J., Arganda-Carreras, I., Frise, E., Kaynig, V., Longair, M., Pietzsch, T., Preibisch, S., Rueden, C., Saalfeld, S., Schmid, B., et al. (2012). Fiji: an open-source platform for biological-image analysis. Nat. Methods *9*, 676–682. https://doi.org/10.1038/nmeth.2019.

83. Yona, S., Kim, K.W., Wolf, Y., Mildner, A., Varol, D., Breker, M., Strauss-Ayali, D., Viukov, S., Guilliams, M., Misharin, A., et al. (2013). Fate Mapping Reveals Origins and Dynamics of Monocytes and Tissue Macrophages under Homeostasis. Immunity *38*, 79–91. https://doi.org/10.1016/j.immuni.2012.12.001.

84. Scheyltjens, I., Van Hove, H., De Vlaminck, K., Kancheva, D., Bastos, J., Vara-Pérez, M., Pombo Antunes, A.R., Martens, L., Scott, C.L., Van Ginderachter, J.A., et al. (2022). Single-cell RNA and protein profiling of immune cells from the mouse brain and its border tissues. Nat. Protoc. *17*, 2354–2388. https://doi.org/10.1038/s41596-022-00716-4.

85. Hartmann, F.J., Bernard-Valnet, R., Quériault, C., Mrdjen, D., Weber, L.M., Galli, E., Krieg, C., Robinson, M.D., Nguyen, X.H., Dauvilliers, Y., et al. (2016). High-dimensional single-cell analysis reveals the immune signature of narcolepsy. J. Exp. Med. *213*, 2621–2633. https://doi.org/10.1084/jem.20160897.

86. Holtmaat, A., Bonhoeffer, T., Chow, D.K., Chuckowree, J., De Paola, V., Hofer, S.B., Hübener, M., Keck, T., Knott, G., Lee, W.C.A., et al. (2009). Long-term, high-resolution imaging in the mouse neocortex through a chronic cranial window. Nat. Protoc. *4*, 1128–1144. https://doi.org/10.1038/nprot.2009.89.

87. Cardona, A., Saalfeld, S., Schindelin, J., Arganda-Carreras, I., Preibisch, S., Longair, M., Tomancak, P., Hartenstein, V., and Douglas, R.J. (2012). TrakEM2 Software for Neural Circuit Reconstruction. PLoS One *7*, e38011. https://doi.org/10.1371/JOURNAL.PONE.0038011.

88. Shen, Z., Lu, Z., Chhatbar, P.Y., O'Herron, P., and Kara, P. (2012). An artery-specific fluorescent dye for studying neurovascular coupling. Nat. Methods *9*, 273–276. https://doi.org/10.1038/nmeth.1857.

89. Young, M.D., and Behjati, S. (2020). SoupX removes ambient RNA contamination from droplet-based single-cell RNA sequencing data. Gigascience *9*, giaa151. https://doi.org/10.1093/gigascience/giaa151.

90. Butler, A., Hoffman, P., Smibert, P., Papalexi, E., and Satija, R. (2018). Integrating single-cell transcriptomic data across different conditions, technologies, and species. Nat. Biotechnol. *36*, 411–420. https://doi.org/10.1038/nbt.4096.

91. Andreatta, M., and Carmona, S.J. (2021). STACAS: Sub-Type Anchor Correction for Alignment in Seurat to integrate single-cell RNA-seq data. Bioinformatics *37*, 882–884. https://doi.org/10.1093/BIOINFORMATICS/BTAA755.

Please cite this article in press as: Van Hove et al., Interleukin-34-dependent perivascular macrophages promote vascular function in the brain, Immunity (2025), https://doi.org/10.1016/j.immuni.2025.04.003

STAR★METHODS

KEY RESOURCES TABLE

REAGENT or RESOURCE	SOURCE	IDENTIFIER
Antibodies		
anti-mouse CD31, clone 390, Brilliant Violet 605	BioLegend	Cat#102427; RRID: AB_2563982
anti-mouse MerTK, clone DS5MMER, Super Bright 780	eBioscience	Cat#78-5751-82; RRID: AB_2762814
anti-mouse CD11b, clone M1/70, Brilliant UltraViolet 661	BD	Cat#565080; RRID: AB_2722548
anti-mouse CD11b, clone M1/70, Brilliant UltraViolet 737	BD	Cat#564443; RRID: AB_2738811
anti-mouse CD11c, clone N418, PE-Cy5.5	eBioscience	Cat#35-0114-82; RRID: AB_46709
anti-mouse CD11c, clone N418, Brilliant Violet 570	BioLegend	Cat#117331; RRID: AB_10900261
anti-mouse CD16/CD32, clone 93, purified	BioLegend	Cat#101310; RRID: AB_2103871
anti-mouse CD206, clone C068C2, Alexa Fluor 700	BioLegend	Cat#141734; RRID: AB_2629637
anti-mouse CD206, clone C068C2, Brilliant Violet 650	BioLegend	Cat#141723; RRID: AB_2562445
anti-mouse CD38, clone 90, Alexa Fluor 488	BioLegend	Cat#102714; RRID: AB_528796
anti-mouse CD45, clone 30-F11, Brilliant UltraViolet 395	BD	Cat#565967; RRID: AB_2651134
anti-mouse CD45, clone 30-F11, Brilliant UltraViolet 563	BD	Cat#565710; RRID: AB_2722550
anti-mouse CD45, clone 30-F11, PE-Cy5	BD	Cat#553082; RRID: AB_394612
anti-mouse CD64, clone X54-5/7.1, PE	BioLegend	Cat#139304; RRID: AB_10612740
anti-mouse CD163, clone TNKUPJ, PerCP-eFluor710	Invitrogen	Cat#46-1631-82; RRID: AB_2716956
anti-mouse CD163, clone TNKUPJ, PE	eBioscience	Cat#12-1631-82; RRID: AB_2716924
anti-mouse Collagen IV, polyclonal	Bio-Rad	Cat#2150-1470; RRID: AB_2082660
anti-mouse CCR2, clone SA203G11, Alexa Fluor 647	Biolegend	Cat#150603; RRID: AB_2566139
anti-mouse CX3CR1, clone SA011F11, Alexa Fluor 488	BioLegend	Cat#149021; RRID: AB_2565704
anti-mouse CX3CR1, clone SA011F11, Brilliant Violet 605	BioLegend	Cat#149027; RRID: AB_2565937
anti-mouse CX3CR1, clone SA011F11, PE-Dazzle 594	BioLegend	Cat#149013; RRID: AB_2565697
anti-mouse CX3CR1, clone SA011F11, Brilliant Violet 510	BioLegend	Cat#149025; RRID: AB_2565707
anti-mouse F4/80, clone CI:A3-1, Alexa Fluor 647	AbD Serotec	Cat#MCA497A488; RRID: AB_323931
anti-mouse F4/80, clone BM8, Brilliant Violet 421	BioLegend	Cat#123137 RRID: AB_2563102
anti-mouse F4/80, clone BM8, Brilliant Violet 510	BioLegend	Cat#123135; RRID: AB_2562622
anti-mouse F4/80, clone BM8, PE-Cy5	BioLegend	Cat#123112; RRID: AB_469740
anti-mouse GR-1, clone RB6-8C5, PE-Cy5.5	BD	Cat#35593182; RRID: AB_394643
anti-mouse I-A/I-E, clone M5/114.15.2, Alexa Fluor 700	BioLegend	Cat#107622; RRID: AB_493727
anti-mouse I-A/I-E, clone M5/114.15.2, Brilliant Blue 700	BD	Cat#746197; RRID: AB_10702819
anti-mouse I-A/I-E, clone M5/114.15.2, PE-Cy5	BD	Cat#107612; RRID: AB_313327
anti-mouse Iba1, clone 019-19741, purified	Wako	Cat#019-19741; RRID: AB_839504
anti-mouse Ly6C, clone HK1.4, Brilliant Violet 711	BioLegend	Cat#128037; RRID: AB_2562630
anti-mouse Ly6G, clone 1A8, Brilliant UltraViolet 563	BioLegend	Cat#565707; RRID: AB_2739334
anti-mouse Ly6G, clone 1A8, Brilliant Violet 650	BioLegend	Cat#127641; RRID: AB_2565881
anti-mouse LYVE1, clone ALY7, eFluor 660	eBioscience	Cat#50-0443-82; RRID: AB_10597449
anti-mouse LYVE1, clone ALY7, purified	eBioscience	Cat#14-0443-82;RRID: AB_1633414
anti-mouse MerTK, clone DS5MMER, PE-Cy7	eBioscience	Cat#25-5751-82; RRID: AB_2573466
anti-mouse FOLR2, clone 10/FR2, APC	BioLegend	Cat#153306; RRID: AB_2721312
anti-mouse NRP1, clone 3E+12, BV421	BioLegend	Cat#145209; RRID: AB_2562358
anti-mouse CD19, clone 6D5, Spark Blue 550	BioLegend	Cat#115565; RRID: AB_2819827
anti-mouse P2Y12, polyclonal, purified	AnaSpec	Cat#AS-55043A; RRID: AB_2298886
anti-mouse Siglec1, clone SER4, eFluor660	eBioscience	Cat# 50-5755-82; RRID: AB_2574241
anti-mouse Tim-4, clone RMT4-54, PE-Cy7	BioLegend	Cat#130009; RRID: AB_2565718
anti-GFP, polyclonal	Nacalai Tesque	Cat#04404-84; RRID: AB_10013361

(*Continued on next page*)

Please cite this article in press as: Van Hove et al., Interleukin-34-dependent perivascular macrophages promote vascular function in the brain, Immunity (2025), https://doi.org/10.1016/j.immuni.2025.04.003

Continued

REAGENT or RESOURCE	SOURCE	IDENTIFIER
anti-mouse O4, clone REA576, PE	Miltenyi	Cat#130-117-711; RRID: AB_2751913
anti-mouse CD13, clone R3-242, FITC	BD	Cat#558744; RRID: AB_397101
anti-mouse CD140a, clone APA5, PE-Cy7	BioLegend	Cat#135911; RRID: AB_2715974
anti-mouse GFAP, clone 2.2B10, purified	Invitrogen	Cat#13-0300; RRID: AB_2532994
anti-mouse AQP4, polyclonal, purified	Novus Biologicals	Cat#NBP1-87679; RRID: AB_11006038
anti-mouse ACE2, polyclonal, purified	R&D	Cat#AF3437; RRID: AB_2223140
anti-mouse IL34, polyclonal, purified	R&D	Cat#AF5195; RRID: AB_2124393
anti-human IL34, clone 1D12, purified	abcam	Cat#ab101443; RRID: AB_10711208
anti-mouse PDGFRB, clone APB5, purified	eBioscience	Cat#14-1402; RRID: AB_467493
anti-human GLUT1, clone EPR3912, purified	abcam	Cat#ab195359; RRID: AB_2714026
goat anti-rabbit polyclonal, Alexa Fluor 647	Thermo Fisher	Cat#A-21244; RRID: AB_2535812
goat anti-chicken polyclonal, Alexa Fluor 488	Thermo Fisher	Cat#A-11039; RRID: AB_2534096
goat anti-rabbit polyclonal, Alexa Fluor 488	Thermo Fisher	Cat#A11034; RRID: AB_2576217
goat anti-rat polyclonal, Alexa Fluor 647	Thermo Fisher	Cat#A21247; RRID: AB_141778
goat anti-mouse polyclonal Podocalyxin	R&D	CAT#AF1556; RRID: AB_354858
goat anti-mouse polyclonal IgG, Alexa Fluor 647	BioLegend	Cat#405322; RRID: AB_2563045
goat anti-rat polyclonal, Alexa Fluor 647	Thermo Fisher	Cat#A21247; RRID: AB_141778
anti-mouse α-Smooth Muscle, clone 1A4, FITC	Sigma	Cat#F3777; RRID: AB_476701
Chemicals, peptides, and recombinant proteins		
Collagenase type IV	Sigma-Aldrich	Cat#C5138-1G
Collagenase A	Sigma-Aldrich	Cat#10103578001
Dispase	Gibco	Cat#17105-041
Corn oil	Merck	Cat#C8267-2.5L
Dextran, Texas Red, 70,000 MW	Thermo Fisher	Cat#D1864
DNAse	Gibco	Cat#17105-041
Escornakon	Streuli	ATCvet-Code: QN51AA01
Evans blue	Sigma Aldrich	Cat#E2129-10G
FBS	Merck	Cat#TMS-013-B
HBSS (with Ca^{2+}/Mg^{2+})	Gibco	Cat#14025-050
M-MLV reverse transcriptase	Invitrogen	Cat#28025
Mounting medium	LubioScience	Cat#SCR-038447
Normal goat serum	Life Technologies	Cat#PCN500
PBS	Homemade	N/A
Percoll	GE	Cat#P4937
PFA 4%, pH 7.4	Morphisto	Cat#11.762
RNeasy Plus Micro Kit	Qiagen	Cat#74034
Tamoxifen	Merck	Cat#T5648-5G
Zombie Near-IR Fixable Viability kit	BioLegend	Cat#423106
Quick-RNA Microprep Kit	Zymo Research	Cat#R1051
PLX5622	Chemgood	Cat#C-152
Critical commercial assays		
SuperScript II Reverse Transcriptase	Thermo Fisher	Cat#18064014
SYBR Green	Bio-Rad	Cat#1725124
Deposited data		
GSE292245, GSE292306, GSE292466	This paper	N/A
Oligonucleotides		
Pol2 forward: CTG GTC CTT CGA ATC CGC ATC	This paper	N/A
Pol2 reverse: GCT CGA TAC CCT GCA GGG TCA	This paper	N/A

(*Continued on next page*)

Please cite this article in press as: Van Hove et al., Interleukin-34-dependent perivascular macrophages promote vascular function in the brain, Immunity (2025), https://doi.org/10.1016/j.immuni.2025.04.003

Continued

REAGENT or RESOURCE	SOURCE	IDENTIFIER
Il34 forward: ACT CA G AGT GGC CAA CAT CAC AAG	This paper	N/A
Il34 reverse: ATT GAG ACT CAC CAA GAC CCA CAG	This paper	N/A
Experimental models: Organisms/strains		
Mouse: *C57BL/6JRj*	Janvier Labs	RRID:IMSR_JAX:000664
Mouse: *Csf1*$^{fl/fl}$	Sherry Abboud Werner (University of Texas Health Science Center)	RRID:IMSR_JAX:021212
Mouse: *Csf1r*$^{fl/fl}$	Jeffrey Pollard (Albert Einstein College of Medicine)	RRID:IMSR_JAX:021212
Mouse: *Cx3cr1*$^{CreER/+}$	Steffen Jung (Weizmann Institute)	RRID:IMSR_JAX:021160
Mouse: *Deleter*$^{Cre/+}$ (*Del*^{Cre})	F. Schwenk (Institute for Genetics, University of Cologne)	RRID:IMSR_JAX:006054
Mouse: *Il34*$^{fl/fl}$	Burkhard Becher (University of Zurich)	N/A
Mouse: *Il34*$^{LacZ/+}$	Burkhard Becher (University of Zurich)	N/A
Mouse: *Mrc1*$^{Cre/+}$	Melanie Greter (University of Zurich)	N/A
Mouse: *Pdgfrb-EGFP*	The Jackson Laboratory	RRID:IMSR_JAX:007669
Mouse: Tbx*18*$^{CreER/+}$	The Jackson Laboratory	RRID:IMSR_JAX:031520
Software and algorithms		
FlowJo v10.8.1	Tree Star	https://www.flowjo.com/
GraphPad Prism 9	GraphPad Software	https://www.graphpad.com/
Imaris 9.2.0	Bitplane	www.bitplane.com/
R	R Development Core Team, 2008	https://www.r-project.org/
R Studio	R Studio, Inc.	https://www.rstudio.com/
UMAP	Brecht et al.[80]	https://github.com/lmcinnes/umap
CellChat	Jin et al.[55]	https://github.com/sqjin/CellChat
Illustrator CS5.1	Adobe	http://www.illustrator.com
FlowSOM	Van Gassen et al.[81]	https://onlinelibrary.wiley.com/doi/10.1002/cyto.a.22625
Fiji	Schindelin et al.[82]	https://www.nature.com/articles/nmeth.2019
MATLAB	N/A	https://ch.mathworks.com/products/matlab.html
Other		
FACSymphony	BD	N/A
Aurora	Cytek	N/A
LSR II Fortessa	BD	N/A
Hyrax C60 Cryostat	Zeiss	N/A
FACSAria III	BD	N/A
FACSymphony S6 5L sorter	BD	N/A
Biological Samples		
Human cortex samples (no cerebral neoplasia after maximum of postmortem interval of 24 h)	University Hospital Zurich	N/A

Please cite this article in press as: Van Hove et al., Interleukin-34-dependent perivascular macrophages promote vascular function in the brain, Immunity (2025), https://doi.org/10.1016/j.immuni.2025.04.003

EXPERIMENTAL MODEL AND SUBJECT DETAILS

Mice

C57BL/6JRj mice were purchased from Janvier Labs. All other mice were bred in-house (see key resources table): *Il34*^{LacZ}, *Il34*$^{fl/fl}$ [19], *Tbx18*^{CreER} (Jackson Laboratory), *Pdgfrb*-eGFP (Gensat.org. Tg(Pdgfrb-eGFP)JN169Gsat/Mmucd), *DTA*, *Csf1*$^{fl/fl}$ were kindly provided by Jean X. Juang (the University of Texas Science Center), *Csf1*$^{-/-}$ (obtained by breeding *Csf1*$^{fl/fl}$ mice with *Del*^{Cre} mice (CMV-Cre, Jackson Laboratory)), *Csf1r*$^{fl/fl}$ (J#021212), *Cx3cr1*^{CreER} mice were kindly provided by S. Jung (Weizmann Institute).[83] All 'Cre' and 'CreER' strains were used as heterozygotes. All animal experiments performed in this study were approved by the Swiss Veterinary Office. All mice were on a C57BL/6 background and housed in individually ventilated cages (IVC) under specific-pathogen-free (SPF) conditions. In general, 2- to 6-month-old mice were used for timed matings, and both female and male embryos and neonates were analyzed.

Generation of Mrc1^{Cre} mice

The transgenic construct was synthesized by GenScript and delivered as a part of pUC57-mini plasmid. It was further amplified using TOP10 *E. coli* strain (Invitrogen), isolated and purified with Maxiprep (QIAGEN). The insertion was performed using CRISPR-Cas9 gene targeting by pro-nuclear injection of linear-dsDNA repair targeting fragment (10 ng/ul) and Cas9 RNP comprised of Cas9 protein (50 ng/ul) and cr:trcrRNA duplex (both form IDT) into fertilized C57BL/6J oocytes. The crRNA targeted the sequence 5'-CCTAATCT GACTGTCTCATATTC-3' just downstream of the *Mrc1* stop codon. The litters were genotyped for the transgenic insertion and backcrossed with C57BL/6J for more than 3 generations. The whole insertion region including surrounding genomic DNA was sequenced to verify correct integration.

Human Tissue Samples

Anonymized brain autopsy tissue from the cerebrum (left temporal region) was obtained from subjects without evidence of cerebral neoplasia and who had provided a general consent (UZS) (3 males, 1 female, median age 65.5. years), within a maximal postmortem interval of 24 hours. The study complied with the guidelines of the Kantonale Ethikkommission (KEK) Zürich (BASEC-Nr. Req-2018-0073) and the Swiss Federal Human Research Act.

Tamoxifen treatment

Tamoxifen was reconstituted with 100% ethanol in corn oil to a final concentration of 25 mg/ml. 5 mg were administered via oral gavage (o.g.) three times every second day to adult mice. Pregnant mice were treated with tamoxifen (o.g.) at E14.5 and E16.5.

METHOD DETAILS

Cell suspension preparation

Mice were euthanized by CO_2 inhalation, and trans-cardiac perfusions were performed with ice-cold PBS. For brain cell suspensions: Embryos were removed from the uterus of the pregnant mice, and the brains, comprising the meninges (pia and dura mater) and choroid plexus, were harvested.

For early postnatal and adult mice, the brain was dissected and, if not mentioned otherwise, only the brain without the dura mater was analyzed. For the brain compartment experiments, the pia mater, choroid plexi from all ventricles, and the dura mater were carefully micro-dissected, as described in.[84] The samples were cut into small pieces in an Eppendorf tube and incubated in digestion buffer (HBSS supplemented with 5% FBS, 2 mM HEPES, and 0.4 mg/mL Collagenase IV (Sigma-Aldrich)) for 20 minutes (embryo) or 40 minutes (adult) while shaking. For embryonic and early postnatal brains, no percoll gradient for leukocyte isolation is required. Samples were washed with ice-cold PBS, filtered through a 70 μm cell strainer, and then stained with fluorescence cytometry antibodies.

Adult brains were homogenized with a syringe and then filtered through a 150 μm cell strainer. This was followed by gradient centrifugation with 30% Percoll (GE Healthcare Life Sciences) in PBS (v/v) (2750 x g for 30 minutes at 4°C without brakes) and subsequently, myelin was removed with a suction pump. Cells were filtered through a 150 μm cell strainer, washed with ice-cold PBS, and centrifuged for 15 minutes at 1500 rpm, 4°C to generate a single-cell suspension. The samples were then ready for staining with fluorescent antibodies.

Preparation of single-cell suspensions for flow cytometry

For spleen, kidney, and lung cell suspensions: Tissues were cut into small pieces, followed by digestion in 0.4 mg/ml Collagenase IV (Sigma-Aldrich) in HBSS supplemented with 2% FCS for 30 min at 37°C. For liver cell suspensions: Livers were cut into small pieces and digested in 1 mg/ml Collagenase A (Sigma) in HBSS with DNAse I (30 μg/ml DNAseI) for 30 minutes at 37° C. After digestion, samples were further homogenized with an 18G needle and syringe and filtered through a 70 μm strainer. The cells were then washed and spun for 8 minutes at 1500 rpm at 4° C. Supernatant was discarded, and the cells were incubated in 1 ml of red blood cells lysis buffer, washed, and stained for flow cytometry analysis.

For skin cell suspensions: Ears were split into two parts and floated epidermal side down on 2.4 mg/ml Dispase (Roche) in HBSS for 1.5 h at 37°C. The skin was then cut into small pieces and incubated in 0.4 mg/ml Collagenase IV (Sigma) and 0.04 mg/ml DNAse I

(Sigma) in HBSS (Gibco) and 10% FBS (Gibco) for 1.5 h at 37°C. After digestion, skin suspension was homogenized with an 18G needle and syringe, filtered through a 100 μm cell strainer, washed with PBS, and stained with antibodies for flow cytometry analysis.

To obtain bone marrow cell suspensions, femurs were flushed with HBSS using a 24G needle, followed by red blood cell lysis for 10 min at 4°C, and washing with PBS and staining with antibodies for flow cytometry analysis.

To obtain small-intestinal lamina propria cell suspensions: the small intestine was harvested and flushed with ice-cold PBS and an 18G gavage needle. The samples were mounted and fat tissue and Peyer's patches were removed. Guts were subsequently fileted open and the luminal side was rinsed with PBS. The samples were incubated at 37°C, 80 rpm for 15 minutes in pre-warmed HBSS (without Ca^{2+}/Mg^{2+}) containing 2% FCS, 10 mM HEPES, 5 mM EDTA and 5 mM DTT. All samples were vortexed for 10 seconds on medium speed and placed into a pre-warmed HBSS (without Ca^{2+}/Mg^{2+}) containing 2% FCS, 10 mM HEPES, 5 mM EDTA and incubated for 10-15 minutes at 37°C, 80 rpm. This step was repeated 3 times. The samples were then transferred into a tube that contained 1 ml digestion buffer (3% FCS, 10 mM HEPES, 30 μg/ml DNAseI, 100 μg/ml Liberase TM, HBSS (with Ca^{2+}/Mg^{2+})) and samples were manually minced. Tissues were incubated for 30 minutes at 37°C at 120 rpm and subsequently processed using the GentleMacs™ tissue dissociator. Homogenate was filtered through a 100 μm cell strainer into FACS buffer. Pellets were resuspended in 1 ml Percoll (40%) and spun down at 2000 rpm for 20 minutes while deceleration was set to 3. The supernatants were aspirated, and the pellets were resuspended into FACS buffer. Afterward, samples were centrifuged, and pellets were resuspended in FACS buffer ready for FACS staining.

Flow cytometry

Cells were incubated with anti-mouse CD16/32 in PBS for 15 minutes to block the Fc receptor. This was followed by washing with PBS and resuspension in the desired antibody mix in PBS. Cell surface staining was performed for 20 minutes at 4°C, and cells were then washed with cold PBS. Afterward, cells were resuspended in FACS buffer (2 mM EDTA, 2% FCS in PBS) and analyzed using an LSR II Fortessa, FACSymphony A5 (BD Biosciences), and FlowJo software (BD) or a Cytek Aurora (Cytek). Cell sorting was performed using a FACSAria III or FACSymphony S6 5L (BD Biosciences. Fluorochrome-conjugated monoclonal antibodies (mAbs) specific for mouse MHCII (I-A/I-E) (clone M5/114.15.2), CD11b (clone M1/70), CD11c (clone N418), CD45 (clone 30-F11), Ly6C (HK1.4), Ly6G (clone 1A8), CD64 (clone X54-5/7.1), F4/80 (clone CI:A3-1), CD206 (clone C068C2), CD38 (clone 90), CX3CR1 (clone SA011F11), GR-1 (clone RB6-8C5), F4/80 (clone BM8), CD163 (clone TNKUPJ), FOLR2 (clone 10/FR2), Tim-4 (clone F31-5G3), NRP11 (3E+12), CCR2 (SA203G11) and MerTK (clone DS5MMER) were purchased from BD Bioscience, eBioscience, AbD Serotec or Biolegend. Duplets were excluded from analysis using SSC-A/H and FSC-A/H, and dead cells were excluded using a near-infrared Fixable Viability Kit (BioLegend).

High-dimensional analysis

Raw data was pre-processed using FlowJo followed by transformation in R, percentile normalization in R obtaining values between 0 and 1, dimensionality reduction, and visualization by UMAP.[80] The FlowSOM algorithm was used for automated clustering[81] using UMAP with overlaid mean marker expression values and a heatmap of median expression values.[8,85] Individual cluster frequencies were computed for each cluster using R, exported into an Excel file, and used for further downstream analysis.

Quantitative RT-PCR (qRT-PCR)

Total RNA was isolated from FACS-sorted cells using the RNeasy Plus Micro Kit (Qiagen) or Quick-RNA Microprep Kit (Zymo Research). cDNA was synthesized using M-MLV reverse transcriptase (Invitrogen), and qRT-PCR was performed on a CFX384 Touch Real-Time PCR Detection System (Bio-Rad) using SYBR Green (Bio-Rad). Primers used in this paper are listed in the key resources table.

PLX5622 administration

Oral CSF-1R inhibitor PLX5622 (Plexxikon Inc., Chemgood) was formulated in AIN-76A standard chow by Research Diets (New Brunswick, NJ) at 1200 ppm. Control mice received AIN-76A chow without PLX5622.

Anesthesia for surgery and two-photon imaging

For surgery, mice were anesthetized with a mixture of fentanyl (0.05 mg/kg body weight; Sintenyl; Sintetica), midazolam (5 mg/kg body weight; Dormicum, Roche), and medetomidine (0.5 mg/kg body weight; Domitor; Orion Pharma), administered subcutaneously. To prevent hypoxemia, a face mask provided 300 ml/min of 100% oxygen. During two-photon imaging, mice were anesthetized with 1.2% isoflurane (Attane; Piramal Healthcare, India) and supplied with 300 ml/min of 100% oxygen. Core temperature was kept constant at 37°C using a homeothermic heating blanket system (Harvard Apparatus) during all surgical and experimental procedures. The animal's head was fixed in a stereotaxic frame (Kopf Instruments) and the eyes were kept moist with ointment (vitamin A eye cream; Bausch & Lomb).

Head-plate and cranial window surgery

The scalp of the mouse was cleaned and disinfected with Kodan (Schülke & Mayr AG). Subsequently, the animal was transferred to a stereotactic frame (Model 900; David Kopf Instruments), and the head was fixated using ear bars. A midline incision of approximately 1.5 cm was made to expose the skull, and the periosteum was gently removed. A bonding agent (Gluma Comfort Bond; Heraeus

Please cite this article in press as: Van Hove et al., Interleukin-34-dependent perivascular macrophages promote vascular function in the brain, Immunity (2025), https://doi.org/10.1016/j.immuni.2025.04.003

Kulzer) was applied to the cleaned skull and polymerized with a handheld blue light source (600 mW/cm^2; Demetron LC). A custom-made steel head-plate was connected to the bonding agent on the skull with dental cement (Synergy D6 Flow; Coltene/Whaledent AG). A 4 × 4 mm craniotomy was then performed above the somatosensory cortex using a dental drill (Bien-Air Dental). A square Sapphire glass coverslip (3 × 3 mm, UQG Optics) was placed on the exposed dura mater and fixed to the skull with dental cement, according to published protocols.[86] The skin lesion was sealed with Histoacryl (B. Braun) and treated with antibiotic ointment (Neomycin, Cicatrex; Janssen-Cilag AG) and closed with acrylic glue (Histoacryl; B. Braun). After surgery, the animals were kept warm and were given analgesics (Temgesic [buprenorphine] 0.1 mg/kg body weight; Sintetica) and pre-warmed Ringerfundin (10 ml/kg; s.c.) to prevent dehydration. Mice were allowed to recover for at least 2 weeks before the start of the imaging session.

Animal habituation for awake two-photon imaging

The training for awake imaging started once the animals fully recovered from the craniotomy. The animals underwent habituation training with the experimenter and the head fixation procedure by gradually increasing the fixation time over several days.

Two-photon imaging

Two-photon experiments were conducted using a custom-built ultra-flexible two-photon laser scanning microscope. Excitation was achieved with a Titanium:sapphire (Ti:sapphire) laser with an adjustable excitation wavelength range of 680–1300 nm, a pulse width of 120 fs, and an 80 MHz repetition rate (Chameleon Discovery TPC; Coherent; Spectra Physics). Prior to imaging, the laser was tuned to the respective wavelength. A 25x water-immersion objective (W Plan-Apochromat 25x/1.05 NA; Olympus) was utilized. The emission light beam was split by a dichroic mirror at 506 nm and 560 nm and further separated into the imaging channels with 535/50 nm and 607/70 nm bandpass filters. The light was collected with photon-multiplier tubes (Fluorescence detection: H10770PA-40 SEL; Hamamatsu; phosphorescence detection: H10770PA-50 SEL; Hamamatsu). PMT gain was controlled through custom LabView software. Images were acquired via ScanImage r3.8.1 (Janelia Research Campus).

Assays to assess BBB integrity

Two-photon imaging

BBB integrity was assessed using fluorescently labeled dextrans of different molecular sizes. First, 50 µl of 70 kDa FITC-dextran (2.5%, Sigma-Aldrich, Cat.No. FD70S) was intravenously injected to collect z-stacks (200 x 200 x 350 µm^3) of the vasculature. Next, 50 µl of a low molecular weight dextran (2.5%, 3 kDa TexasRed-dextran (ThermoFisher, Cat.No. D1830)) was intravenously injected. Further z-stacks were then acquired at 0, 5, 10, 15, and 90 min post-injection of low molecular weight dextran. BBB leakage can be observed as the presence of low-molecular-weight dextran in the perivascular space surrounding vessels.

Evans blue

100 µl of Evans blue (2%, in PBS) was injected intraperitoneally. After 18 hours, mice were euthanized with an overdose of Eucanosoid followed by cardiac perfusion with cold PBS. Brains were homogenized using a tissue dissociator in a 50% trichloroacetic acid (Sigma, Cat.No. T6399) solution, diluted in 0.9% Saline (Braun, Cat.No. 534532) and the resulting homogenate was centrifuged for 15 minutes at 2000 g. The supernatant was centrifuged for 15 minutes at 9300 g, after which the supernatant was diluted 4 times in 95% Ethanol. Evans blue fluorescence was measured at excitation/emission wavelengths of 620/680 nm in a Tecan reader.

Immunofluorescence and image processing

Mice were euthanized with CO_2 inhalation, and trans-cardiac perfusions were performed with PBS (4°C). Directly after dissection, mouse brains were fixed for 4-6 hours with 4% paraformaldehyde (PFA) at 4°C. Brains were rinsed with PBS and either cryoprotected with 30% sucrose (w/v in PBS) for 48 hours at 4°C or stored in PBS-Azide for further processing with the cryotome (60-80 µm sections). Samples for cryosectioning were embedded in OCT (Medite) and sectioning was performed with a thickness of 60-80 µm (free-floating) using a Hyrax C60 cryostat (Zeiss). Brain sections were permeabilized by incubation in a blocking solution (PBS supplemented with 2% goat serum and 0.1% Triton X-100) for 1 hour at room temperature (RT). Free-floating sections were stained with primary antibodies at 4°C for 2-3 days using anti-Iba1 (1:500, Wako), anti-CD206 (1:200, LubioScience), anti-CD163 (1:200, eBioscience), anti-Collagen IV (1:400, Bio-Rad), anti-P2Y12 (1:400, Ana Spec), anti-SMA (1:200, Sigma), anti-MHCII (1:100, BioLegend), anti-CD64 (1:200, Bio-Rad) and anti-CD13 (1:100, BD Biosciences), anti-LYVE1 (1:100, eBioscience), anti-IL34 (1:100, R&D), anti-GFP (1:200, Nacalai Tesque), anti-CD31 (1:200, BD Biosciences). After washing three times for 5 minutes each in PBS, samples were incubated for 2 hours at RT with DAPI (1:1000, Thermo Fisher) and the respective secondary antibodies (anti-rabbit, anti-rat, etc., all 1:500). The washing steps were repeated, and sections were mounted with 1 drop of mounting medium (Dianova). High-resolution images were taken using an SP5 upright confocal microscope (Leica) with a 20x emulsion objective with 1024x1024 pixels. Images were acquired in frames with a line average of 16 or 32. DAPI and AF546/AF555 were detected in one sequence and AF488 and AF647/AF660 in a second sequence to avoid spillover. Images were processed and later merged using Imaris imaging software (Bitplane).

Immunofluorescence of brain-derived whole mounts

Whole mounts of the dura mater were obtained by carefully removing it from the skull cap after PFA perfusion of the animals. Samples of the leptomeninges were harvested by cutting a thin slice of the dorsal cortex using a 0.25 mm disposable blade. Afterward, whole

Please cite this article in press as: Van Hove et al., Interleukin-34-dependent perivascular macrophages promote vascular function in the brain, Immunity (2025), https://doi.org/10.1016/j.immuni.2025.04.003

mounts were post-fixed in ice-cold PFA (4%) for 2-2.5 h followed by 2 washing steps with PBS at RT. The samples were further processed as described in "immunofluorescence and image processing".

Transmission electron microscopy

Mice were transcardially perfused under anesthesia (Eucanosoid) with ice-cold PBS followed by freshly made Karnovsky's fixative: 2% PFA (Polysciences, #18814-10), 2.5% glutaraldehyde (Polysciences, #01909-10) in 0.1 M cacodylate buffer (pH 7.4) (Polyscience, #18661-500). Brains were dissected and kept in Karnovsky's fixative until sample preparation for EM. Vibratome sectioning was done to obtain 100 μm coronal sections or horizontal sections, which were washed in 0.1M cacodylate buffer before incubation with 1% OsO_4 for 1 hour in 0.1 M cacodylate buffer, and 1% aqueous uranyl acetate overnight. Samples then were dehydrated in an ethanol series and embedded in Epon/Araldite (Sigma-Aldrich). Ultrathin (70 nm) sections were post-stained with lead citrate and examined with a Talos 120 transmission electron microscope at an acceleration voltage of 120 KV using a Ceta digital camera and the MAPS software package (Thermo Fisher Scientific). We used a Python script to generate a position list of the XYZ coordinates for the tiff images which allowed us to load the tiff images into the plugin TrakEM2[87] in Fiji.[82] Alignment of the tiles was done with TrakEM2.

Immunofluorescent staining on brain vibratome slices

Mice were deeply anesthetized with Eucanosoid and transcardially perfused with ice-cold PBS followed by ice-cold 4% paraformaldehyde (PFA) in PBS, pH 7.2. The brain was removed and post-fixed for 6 hours in 4% PFA in PBS at 4°C with shaking. Brains were sectioned with a vibratome (Leica VT1000S) into 60 μm thick slices and stored in 24 well plates in 0.01% NaN_3 in PBS. Brain slices were blocked overnight in 1% bovine serum albumin (BSA), 0.1% Triton™ X-100 in PBS at 4°C. Followed by an incubation for 3 days at 4°C in a primary antibody cocktail in 0.5% BSA, 0.05% Triton™ X-100 in PBS. The following primary antibodies were used: anti-Collagen IV (1:400, Bio-Rad), anti-SMA (1:200, Sigma), anti-AQP4 (1:300, Novus biologicals), anti-GFAP (1:600, Invitrogen), anti-ACE2 (1:100, R&D systems), anti-PDGFRB (1:50, eBioscience) and anti-Podocalyxin (1:100, R&D systems). Brain slices were washed 4-5 times with 0.5% BSA, 0.05% Triton™ X-100 in PBS at RT. Slices were incubated overnight at 4°C with secondary antibodies diluted in 0.5% BSA, 0.05% Triton™ X-100 in PBS. After this, slices were stained with DAPI, followed by washing in PBS 4-5 times and mounted in ProLong® Gold Antifade (Invitrogen). Immunofluorescent stainings were imaged using a confocal microscope (Leica SP8, objectives - 20× NA (numerical aperture): 0.7). Images were analyzed with Fiji. The following formula was used to calculate the fluorescence intensity: Intensity = RawIntDen of ROI – (background RawIntDen per pixel X area of ROI).

X-Gal staining and immunohistochemistry

Tissues were fixed in 2% formaldehyde/0.2% glutaraldehyde for 1 hour and subsequently stained in X-Gal solution (1 mg/mL X-Gal (Sigma), 2 mM $MgCl_2$, 5 mM K3Fe(CN)6, 5 mM K4Fe(CN)6, 0.02% NP-40, 0.01% sodium deoxycholate) for 14-16 hours at 37°C. Afterward, tissues were fixed in HOPE® I (DCS Innovative Diagnostic-System) for 72 hours followed by embedding in paraffin. Sections were cut and counterstained with Nuclear Fast Red Solution (Sigma). Images were acquired with a brightfield microscope (Olympus).

Laser speckle contrast imaging

Before isoflurane anesthesia, buprenorphine analgesic (0.1mg/kg) was injected subcutaneously. Mice were anesthetized with 4% isoflurane at induction and with 1.5% isoflurane for maintenance. Anesthesia gas consisted of isoflurane mixed with oxygen and medical air at flow rates of 0.2 L/min and 0.8 L/min, respectively. The skin on top of the mouse skull was opened to expose the underlying skull and reduce light scattering. Cortical perfusion imaging was performed using a moorFLPI imaging system (Moor Instruments). Cerebral blood flow (CBF) was measured for 5 minutes in the whole brain. CBF images are generated with arbitrary units in a 256-color palette by the moorFLPI software, and the absolute CBF perfusion units averaged across both hemispheres for mice were measured.

Transcranial widefield localization microscopy

Mice were anesthetized as above (laser speckle contrast imaging). Mice were fixed on the stereotaxic frame and placed on the microscope stage. Orange-yellow fluorescent beads (FMOY-1.3, 460/594 nm, Cospheric) were diluted in PBS and administered intravenously through the tail vein, and images were acquired in the far-red emission channel (647 nm). The frame rate of the camera was set to 200 Hz to record the entire injection process, which lasted 5 seconds. Exposure time was held constant throughout the duration of the imaging sequence and across the experimental group. The flow of fluorescent beads into the brain vasculature was imaged with a customized compromising sCMOS camera (pco.dimax S1, PCO AG) and a 473 nm CW laser (FPYL-473-1000-LED, Frankfurt Laser Company). Imaging sequences were initiated, processed, and analyzed using MATLAB (MathWorks). Density maps of the fluorescent beads were computed by counting all the positions detected in one pixel during the acquisitions.

Vasomotion measurements

Spontaneous vasomotion was detected using *in vivo* two-photon microscopy in trained awake head-fixed mice. To differentiate arteries from veins, we injected 100 l of AlexaFluor 633 hydrazide (ThermoFisher, Cat.No. A30634) intravenously via the tail vein at least 1 hour before awake imaging.[88] Spontaneous vessel dilations and constrictions in pial arteries and arterioles were continuously

recorded over a 5-minute time course. Power spectral density analyses of these recordings revealed peaks centered around 0.1 Hz. Peak-vessel dilations were determined using the *findpeaks* function in MATLAB, with peak prominence defined as dilation events lasting at least 3 seconds.

Blood pressure and gas analysis

Blood pressure was measured with the BP 2000 Blood Pressure Analysis System (Visitech Systems; Apex, NC) according to the manual instructions. 3-month-old male and female mice (n=12) were used. Experiments were performed between 9 am and 12 pm. Mice were acclimated to restraint and tail-cuff inflation for 4 days before the experiment on day 5. The restraint platform was maintained at 38°C. For each animal, 10 preliminary measurements were carried out before the actual 30 measurements. For each animal, 8 to 22 readings were accepted out of the 25 to 30 successful measurements by the software (BP-2000 Software Version January 12th 2017).

For blood gas analysis, mice were anesthetized with isoflurane using air as vehicle gas to maintain normal pO_2. Blood was collected retroorbitally and blood gases and electrolytes were measured immediately with a blood-gas analyzer (Epoc blood gas analysis system, Siemens, Germany).

Single-cell RNA sequencing and data analysis

10,000 cells per sample, pooled from 4 animals per genotype, were loaded into 10x Genomics Chromium, and library preparation was performed according to the manufacturer's instructions (Chromium Next GEM Single Cell 3' Reagent kits v3.1 protocol). The libraries were sequenced on a NovaSeq sequencer in line with 10x Genomics recommendations (paired-end reads) with a depth of 50,000 reads per cell. Cell Ranger software (10x Genomics, v.3.1.0) was used to demultiplex, process raw data, and align the reads to the GENCODE reference build GRCm38.p6 Release M23, followed by summarizing the unique molecular identifier (UMI) counts. A filtered gene-cell count matrix was generated by Cell Ranger's built-in cell-calling algorithms.

Additionally, we applied SoupX to remove ambient RNA from the samples, following the workflow described in its original publication.[89] First, ambient mRNA expression profiles obtained from empty droplets were estimated. Second, the contamination extent was identified in each cell by estimating the fraction of UMIs derived from the background. Third, the expression of each cell using an ambient mRNA expression profile was corrected and used for further analysis. Next, we followed the Seurat v3 workflow.[90] Cells with ncount < 500 and nFeature_RNA > 7000 with a mitochondrial cut-off < 20 were excluded. For clustering, a resolution of 0.1 was chosen for the unsupervised cell clustering algorithm, and cell clusters were visualized by UMAP.

Astrocytes and ECs (as internal control) from adult *Il34*$^{LacZ/+}$ and *Il34*$^{LacZ/LacZ}$ littermates were sorted and sequenced in a separate experiment. Sequencing data obtained from this experiment were integrated using STACAS anchors according to the published pipeline.[91] To include all features, the argument features.to.integrate was set to genes that were detected in both datasets.

Datasets obtained from *Il34*$^{LacZ/LacZ}$ and *Mrc1*^{Cre} mice were integrated in the same way as astrocytes and other cell types from the *Il34*$^{LacZ/LacZ}$ datasets. Differentially expressed genes were calculated using Seurat FindMarkers between cells from KO animals and integrated cells from both HET and WT animals. Venn diagrams were drawn using the ggvenn package and included all genes with an adjusted p-value < 0.05.

Ligand-receptor interaction analysis with CellChat

Cell-cell communications were analyzed by applying the R package CellChat developed from.[55] Data obtained from scRNA-seq was processed and the CellChat object was initialized. Next, the ligand-receptor interaction database was set and the expression data was further preprocessed for cell-cell communication analysis. Afterward, the communication probability was computed, and the cellular communication network was inferred. Heatmap visualization was utilized to display the overall signaling pathways of PVMs, VSMCs, pericytes, endothelial cells, and fibroblasts derived from *Il34*$^{LacZ/+}$ and *Il34*$^{LacZ/LacZ}$ mice.

QUANTIFICATION AND STATISTICAL ANALYSIS

Statistical analysis

Statistical analysis (including mean values, SEM values, and *p*-values) was performed using GraphPad Prism 9. Statistical significance between the two groups was evaluated by a two-tailed unpaired Student's *t*-test. Welch's correction was applied in case of significantly different variances. *p*-values below 0.05 were considered as significantly different (*$p < 0.05$; **$p < 0.01$; ***$p < 0.001$; ****$p < 0.0001$ ns, not significant). Mean (±SEM) was indicated with horizontal lines. n represents the number of biological replicates unless otherwise stated. Statistical details for each experiment can be found in the corresponding figure legends.

Biorender was used for part of the Graphical Abstract.